



## Hydrometeorological controls and social response for the ~~22~~-October 2019 catastrophic flash flood in Catalonia, north-eastern Spain

Arnau Amengual<sup>1</sup>, Romu Romero<sup>1</sup>, María Carmen Llasat<sup>2</sup>, Alejandro Hermoso<sup>3</sup> and Montserrat Llasat-Botija<sup>2</sup>

5 <sup>1</sup>Grup de Meteorologia, Departament de Física, Universitat de les Illes Balears, Palma, Mallorca, Spain.

<sup>2</sup>GAMA, Departament de Física Aplicada, Universitat de Barcelona, Barcelona, Spain

<sup>3</sup>Institute for Atmospheric and Climate Science, Department of Environmental Systems Science, Swiss Federal Institute of Technology Zurich, Switzerland

*Correspondence to:* Arnau Amengual ([arnau.amengual@uib.es](mailto:arnau.amengual@uib.es))

10 **Abstract.** On 22 October 2019, the Francolí river basin in Catalonia, north-eastern Spain, experienced a heavy precipitation event that resulted in a catastrophic flash flood, causing six fatalities. ~~Firstly~~, this study investigates the hydrometeorological factors that concurred in the unfolding of this event by using large-scale meteorological grid analyses, high-resolution mesoscale model simulations, radar-derived precipitation estimates, post-flood field observations and hydrological modelling. Mesoscale diagnosis reveals that a persistent south-easterly airflow brought low level moisture and established convective  
15 instability over the region, while local orography was instrumental to trigger moist deep convection. A convective train promoted intense, copious and prolonged precipitation over the north-western catchment headwaters. Basin response was significantly modulated by the very dry initial soil moisture conditions. After the long-lasting rainfall, an acute burst of precipitation resulted in extreme flash flooding. Fast and abrupt increases in river flow lead to short times for protection  
20 procedures to be implemented effectively. ~~Secondly~~, this study collects the social response times during the event and compares them with catchment dynamics. The idea is to examine the adequacy of monitoring and warning issuance in meeting the needs of the population at risk. Based on this information, the study provides recommendations aimed at minimizing losses and improving preparedness for similar natural hazards in the future.



## 30 1 Introduction

**Flash floods** are a highly destructive natural hazard in terms of economic and human losses in the Mediterranean region. According to Llasat et al. (2010), 185 episodes were registered during the 1990-2006 period, resulting in a death toll of 4500 and damage exceeding EUR 29 billion. Petrucci et al. (2019) identified a total of 812 floods in Europe during the 1980-2018 period, resulting in 2466 fatalities. Most of flash flood events occurred in countries located in the Mediterranean  
35 region. The International Disaster Database (EM-DAT) of the Centre for Research on the Epidemiology of Disasters lists a total of 122 episodes related to **floods** and flash floods in Southern Europe for the 1953-2022 period. These natural disasters caused a death toll of 3020 and adjusted-inflation economic damages close to **EUR 60 billion** (<http://www.emdat.be/>).

Besides being a region with a high frequency of flash flooding, the associated social risks are steadily increasing due to an enhanced vulnerability connected with human activities and global warming. On the one hand, intense economic activity  
40 and high population density in the Mediterranean coastal fringe increase the potential of flash flood-related casualties and damages. On the other hand, the Mediterranean region is one of the hotspots for **climate change impacts** (Diffenbaugh and Giorgi, 2012; Paeth et al., 2017; Cramer et al., 2019; Tuel and Eltahir, 2020).

Mediterranean Spain is prone to flash floods during late summer and autumn, recurrently experiencing heavy precipitation episodes (HPEs). **Several factors contribute to the occurrence of these flash flood-producing HPEs.** Firstly, the  
45 relatively high sea surface temperature serves as a source of heat and moisture for the lower layers of the atmosphere. Secondly, the arrival of mid-level cold troughs promotes the advection of warm and moist air masses from the maritime environment, resulting in strong convective instability with high convective available potential energy (CAPE). Thirdly, the complex topography of the Spanish Mediterranean region plays a significant role in channelling low-level jets and initiating deep and moist convection through mechanical uplift. The prominent orography anchors the convective systems, which are continuously  
50 fuelled by high moisture convergence. The combination of all these factors leads to the development of quasi-stationary HPEs that tend to persist over specific areas (Romero et al., 2000; Llasat et al., 2003; García-Herrera et al., 2005; Martín et al., 2007; Pastor et al., 2010; Hermoso et al., 2021).

Given the complex topography of ~~the coastal region,~~ numerous small-to-medium semi-arid basins are scattered along the coastal fringe (Fig. 1). Most of these catchments are ephemeral in nature and are highly responsive to HPEs. Basin response



55 occurs within few hours, reacting with an acute spatial and temporal variability to heavy precipitation. On the one hand, moist deep convection can trigger large rainfall rates and amounts, which inherently feature high heterogeneity in both space and time. On the other hand, thin and poorly-developed soils, limited vegetation cover, steep slopes and urbanization can contribute to the generation of fast and high infiltration-excess runoff rates and surface flows. Following the long dry and warm summer, the occurrence of extreme precipitation intensities and amounts can easily surpass the initially high soil infiltrabilities. The  
60 combination of all these factors can result in the sudden formation of flood bores, which rapidly route through normally dry river beds, leading to catastrophic effects downstream (Amengual et al., 2007 and 2015; Roca et al., 2009; Martín-Vide and Llasat, 2018; Lorenzo-Lacruz et al., 2019).

Basin response to extreme flooding is linked to drainage size and runoff triggering. As the catchment area decreases, the time reduction in basin response implies that people are more exposed to flash flood-related risks: Individuals are not so  
65 protected by structural measurements and non-structural polices for flash flood defence become more crucial (Creutin et al., 2009). For instance, Ruin et al. (2008) reported that half of the 23 fatalities during the September 2002 widespread flash flooding in the Gard region, France, occurred on drainage areas around 10 km<sup>2</sup>. Lorenzo-Lacruz et al. (2019) found that the 13 fatalities during the October 2018 catastrophic flash flood in Mallorca, Spain, occurred in basin sizes less than 25 km<sup>2</sup>. In such small drainage areas, hydrometeorological monitoring and forecasting should provide warnings with the shortest lead  
70 times as possible after the onset of the flash flood-producing HPEs. This would enable a structured response in form of pre-established defence actions, such as closure of secondary roads, redirection of traffic to secured routs, evacuation of residents in flood-prone areas to safer zones or deployment of emergency personnel.

Flash flood monitoring and forecasting build on the relationship between catchment and social response times (Creutin et al., 2009). When the catchment response time is larger than the social response time, hydrological and/or hydraulic models  
75 can provide forecasts at the required lead times. Otherwise, flash-flood forecasting and warning issuance rely on quantitative precipitation estimates (QPEs) derived from radar observations and/or quantitative precipitation forecasts (QPFs) from high-resolution numerical weather prediction (NWP) models. QPEs-driven runoff simulations can provide forecasts with lead times of a few hours ahead, depending on hydrological response. Short-range NWP models coupled with hydrological models can extend the forecast lead times to 24–48 h (Cloke and Pappenberger, 2009; Hapuarachchi et al., 2011; Wu et al., 2020).





80 ~~In order~~ to gain insight into the hydrometeorological factors relevant to flash flooding in Mediterranean Spain and the social response to such events, **a case study is analysed**. The case study took place on 22 October 2019, with observations revealing a maximum 10-min rainfall accumulation of approximately 21.0 mm, and a total amount of 299.5 mm. Subsequent flash flooding devastated the upper Francolí basin in Catalonia, north-eastern Spain (Fig. 1). The event resulted in a death toll of 6 inside the Francolí basin, and the destruction of several dwellings and three bridges along the river. This flash flood was  
85 characterized by the significant amount of woody debris carried by the water, leading to the formation of large jams at various bridges along the river. The anomalous and short-lived peak flow caused by the collapse of a debris jam on one of the bridges produced two of the six fatalities. The regional water authority is now warning flood planners about the potential for catastrophic floods in the valley towns situated along vegetated, torrential basins, particularly if their narrow bridges are susceptible to woody debris (Martín-Vide et al., 2023).

90 The 22 October 2019 HPE serves as a prototype case for well-organized and quasi-stationary convective systems, which are often responsible for the most catastrophic flash floods in Mediterranean Spain. This study aims to examine the primary hydrometeorological factors that contributed to the unfolding of this extreme event. To achieve this goal, large-scale meteorological grid analyses, high-resolution NWP modelling, QPEs obtained from weather radar observations, rain- and stream-gauge measurements, post-event field observations by Martín-Vide et al. (2023), and hydrological modelling are used.  
95 The specific objectives are: (i) ~~to~~ identify the leading physical mechanisms responsible for the onset and evolution of the convective systems; (ii) ~~to~~ investigate the main features of the HPE over the Francolí catchment, and; (iii) ~~to~~ assess basin response to the torrential rainfall.

~~Finally,~~ this study poses particular attention to the relationship between catchment dynamics and social response times. It aims to identify and compare the spatial scales and timing of various social actions with the spatiotemporal catchment  
100 response during the course of the flash flood. This comparison would allow to assess whether the existing social protocols are effective in meeting the requirements of the population at risk, both in terms of evaluating flood severity and implementing appropriate mitigation actions. By examining the alignment between catchment and social response, this research seeks to provide insights into the adequacy of current protocols and identify potential areas for improvement in the management of catastrophic flash flooding.



## 105 2 Case study

### 2.1 The study area

#### 2.1.1 The Francolí catchment: an overview

The Francolí basin covers an area of 858 km<sup>2</sup>, and its river stretches up to 60 km until it reaches Tarragona city (Fig.1). The north-western part of the catchment is shaped by the Catalanian prelitoral mountainous ranges, reaching a maximum elevation ca 1200 m and featuring bed slopes of up to 2.0%. As being hydraulically disconnected of the underlying aquifers, the Francolí river is characterized by a very irregular and torrential flow regime, relying on rainfall. Its mean annual flow is 1.2 m<sup>3</sup>s<sup>-1</sup>, but it is occasionally subjected to hazardous flash floods. The most catastrophic episodes on record took place on 23 September 1874, 18-19 October 1930, and 10 October 1994 (Roca et al., 2009).

The upper Francolí watershed settles over poorly resistant tertiary materials consisting of detritic loam, gypsum and limestone. The western mountain ranges are primary composed of slate, granite, limestone, sandstone and clay bedrock. Thin and poorly developed lithosoils are predominant on this relief, while the river valley is dominated by more developed clay loam or silt loam soils (Barettino and Pujadas, 1992). Underlying most of the area is a plioquaternary detritic aquifer, mainly composed of silts, sands and gravels (Postigo et al., 2010; Sendròs et al., 2014).

The Brugent river is the main left tributary that flows into the upper Francolí basin (Fig. 1). The Brugent basin lays over extensive karstified limestone, carbonate and dolomitic fractured bedrock, which promotes high infiltration rates and facilitates the recharge of deep calcareous aquifers (Pujadas, 1994). The mountains sustain a deciduous forest, while pine trees dominate at lower elevations. The river valley is devoted to rainfed agriculture, with grapevines and cereals being the primary crops. Several small towns with populations exceeding 8.000 inhabitants are located on the valley plains of the upper basin, in close proximity to the river.

#### 125 2.1.2 The observational networks

The Francolí river is monitored by the Catalan Water Agency (ACA) at two cities: Montblanc (339.9 km<sup>2</sup>) and Tarragona (809.1 km<sup>2</sup>). Raw streamflow data is collected by the automatic stream-gauge stations with a temporal resolution of 5-min (Fig. 1). However, the flood bore destroyed the stream-gauge in Montblanc, resulting in the unavailability of a



complete time series of data for the 22 October 2019 episode. Automatic raw precipitation data is recorded by several agencies  
130 at different temporal frequencies across Catalonia.

The Catalan Meteorological Service (SMC) operates 172 pluviometers with a 10-min frequency. The Spanish Agency  
of Meteorology (AEMET) has 62 rain-gauges with a 10-min temporal resolution in Catalonia. The Meteoprades amateur  
association maintains 17 stations with a 5-min time-step. Out of these 251 stations, 59 are located inside or very close to the  
Francolí catchment. Additionally, daily rainfall amounts are recorded by AEMET in 212 additional and independent rain  
135 gauges across Catalonia, 48 of them situated inside or near the basin. The region is also monitored by the SMC XRAD radar  
network, and the AEMET Doppler C-band weather radar. The AEMET radar is deployed in close proximity to Barcelona city,  
approximately 60 km away from the Francolí catchment, and it is used in this work (Fig. 1).

## 2.2 Synoptic situation

Prior to the onset of the convective episode in Catalonia, the synoptic evolution was characterized by the presence of  
140 an intense Potential Vorticity (PV) streamer progressing towards the Atlantic coast of the Iberian Peninsula at upper levels  
(Fig. 2a). The PV streamer reached values of more than 8 PVU ( $1 \text{ PVU} = 10^6 \text{ Km}^2 \text{ s}^{-1} \text{ kg}^{-1}$ ) at 250 hPa. In correspondence with  
this upper-level dynamic structure, a deep trough with cold air could be identified at mid-tropospheric levels. During the  
following hours, the PV streamer tilted eastwards while eventually breaking from the main circulation and forming a closed  
centre over the southern half of the Iberian Peninsula on 23 October 00:00 UTC. Correspondingly, the mid-tropospheric  
145 disturbance adopted the structure of a cut-off cyclone with a cold core (Fig. 2b). Previous studies have indicated that the  
forward flank of such PV streamers provides favourable regions for the development of deep moist convection (Doswell et al.,  
1998; Schumann and Roebber, 2010). The presence of these upper-level anomalies not only contributes to the dynamical uplift  
through the advection of PV, but it also leads to the convective destabilization of the tropospheric column. This destabilization  
is achieved by the intrusion of cold air aloft, which sets up steep lapse rates within the domain of the trough.

150 At low levels, the synoptic situation was also highly supportive of the upward dynamical forcing and convective  
destabilization of the vertical profile, particularly along the Mediterranean coasts of Spain (Figs. 2c and d). The low-level  
thermal structure was characterized by the intrusion of cold air over the Iberian Peninsula, along with the upper-level PV  
streamer, together with the genesis of a marked temperature gradient towards the western Mediterranean.



Cyclogenesis took place over the Balearic Islands, that is, in the forward flank of the upper-level PV anomaly as it  
155 tilted and closed. The circulation associated with the surface cyclone contributed to the strengthening of the thermal front and  
the advection of warm and moist Mediterranean air towards Catalonia. **The evolution of this baroclinic structure at low levels  
was instrumental to promote upward vertical motion and the destabilization of the low-level air parcels.** In addition, once the  
convective systems formed, this circulation pattern ensured a continuous supply of warm and moist air conveyed over the  
Mediterranean waters, which still feature high sea surface temperatures in autumn. Similar mechanisms have been observed  
160 in other flash flood episodes in the Spanish Mediterranean region, where flash flood-producing HPEs occurred in the  
overlapping area between the forward flank of an upper-level anomaly, and a lower-level warm and moist easterly jet with a  
large course over the Mediterranean Sea (Amengual et al., 2015; Hermoso et al., 2021).

### 3 Methods

#### 3.1 Mesoscale atmospheric modelling

165 Regarding the mesoscale numerical simulation of the HPE, the new Triangle-based Regional Atmospheric Model  
(TRAM) is applied. TRAM has been completely developed by the **UIB** team, being a non-hydrostatic and fully-compressible  
meteorological model (Romero, 2023). TRAM is no more than the 3D version –now endowed with a full set of physical  
parameterizations– of an earlier 2D prototype presented in Romero et al. (2019). Advection terms in TRAM are solved using  
a **Reconstruct-Evolve-Average strategy** (Leveque, 2002) over the computational cells. These cells consist of equilateral  
170 triangles in the horizontal. The classical z-coordinate is used in the vertical, allowing arbitrary stretching (e.g. higher resolution  
in the Planetary Boundary Layer (PBL)). Proper treatment of terrain slopes in the bottom boundary conditions allows for  
accurately representing the orographic forcing. To gain computational efficiency, time-splitting is used to integrate separately  
fast and slow terms (e.g. Wicker and Skamarock, 1998), while acoustic modes in the vertical are solved implicitly. The Lambert  
map projection is used, and all Coriolis and curvature terms are retained in the equations. No explicit filters are needed.

175 Regarding the physical parameterizations of cloud microphysics, cumulus convection, short and long-wave radiation,  
PBL processes and surface fluxes, TRAM adopts the “Reisner 2”, “Kain-Fritsch 2”, “Cloud”, “MRF” and “5-layer soil”  
schemes, respectively, from the PSU/NCAR MM5 modelling system (Dudhia, 1993; Grell et al., 1995). Through a large



collection of tests TRAM has shown to perform as well as state-of-the-art numerical models and to be suitable to simulate circulations ranging from small-scale thermal bubbles (~ 100 m scale) to synoptic-scale baroclinic cyclones (> 1000 km size), including orographic circulations, thermally-driven flows, squall lines, supercells, all kinds of precipitation systems and medicanes (Romero, 2023). The model is currently fully operational, providing regional forecasts at different resolutions; twice daily these forecasts are disseminated in the web (further information at <https://meteo.uib.es/tram>).

The basic idea is to explore the numerical predictability of this episode and to describe the leading physical mechanisms responsible for the onset and evolution of the convective systems. Accordingly, the TRAM model was previously submitted to several sources of external large-scale analysis, domain sizes, time horizons and various vertical and horizontal resolutions in order to optimize its performance in terms of the QPF. Finally, TRAM simulations are performed over the western Mediterranean domain shown in Figs. 4 and 5, starting on 22 October 2019 at 00:00 UTC and extending for 48 h, until 24 October 2019 00:00 UTC. The simulations are forced with the ERA5 grid reanalyses. In the vertical 61 computational levels are used, with a thickness increasing from 25 m near sea level to about 400 m in the upper troposphere (model top is located at 16 km). Horizontally, the resolution of the mesh –in terms of the side length of the triangular cells– are set at 4.5 km, with parameterized moist convection. Note that referring to a traditional square-based mesh, this resolution is equivalent to 3 km.

### 3.2 Quantitative precipitation estimates

QPEs are derived from the reflectivity volume scans of the Barcelona Doppler C-band radar of AEMET during the period of 22 to 24 October 2019 at 00:00 UTC (Fig. 1). The radar has a spatial resolution of 1 km in range and 0.8° in azimuth. A complete volume scan is conducted every 10 min, covering a maximum range of 240 km. As volume-scanning is affected by complex terrain, partial beam occlusion is amended by simulating the blocked percentage of beam power. The correction for partial beam occlusion is performed by numerically modelling the propagation of the radar beam over a high-resolution digital terrain model (Pellarin et al., 2002). Furthermore, the signal attenuation caused by heavy rainfall is corrected using the Mountain Reference Technique (Bouilloud et al., 2009). Finally, the quantitative rainfall estimates are obtained by applying the standard WSR-88D convective rainfall rate-reflectivity relationship (i.e.,  $Z=300R^{1.4}$ ; Hunter, 1996; Fulton et al., 1998).





Due to the inherent uncertainties in radar quantitative precipitation estimation (e.g., Gochis et al., 2015), additional inaccuracies in the hourly cumulative rainfall and patterns are amended by using a dynamical fitting technique to the automatic pluviometers (Fig. 3; Cole and Moore, 2008). To further ensure the reliability of the radar-derived precipitation estimates, an independent safety check is performed by comparing the 48-h radar-derived precipitation against observations from the independent AEMET daily pluviometers (Fig. 3). The **statistical comparison** between both databases shows a strong positive correlation over the selected area, with a  $R^2$  of 0.89. Overall, the QPEs exhibit a **very** slight average underestimation of 2.8%.

### 3.3 Hydrological modelling

The event-based and fully-distributed Kinematic Local Excess Model (KLEM; Da Ros and Borga, 1997) is implemented to analyse hydrologic response. KLEM takes into account for properties in topography, soil and vegetation. The Soil Conservation Service-Curve Number method (SCS-CN; USDA, 1986) is used to compute runoff from precipitation. The drainage network is identified using a threshold area procedure, which helps characterize both hillslope and channelized flow paths. The response of the drainage system is then described to represent runoff routing (Giannoni et al., 2003). The routing of surface and channel flows through the drainage structure is completely translational, relying on two invariant velocities along the hillslopes ( $v_h$ ) and channels ( $v_c$ ). In addition, the hydrological model also simulates baseflow by using a linear conceptual reservoir based on the Horton-Izzard equation (Moore and Bell, 2002).

Landscape morphologies and soil properties are described by a 25-m grid size cell. Curve numbers are derived from lithology and land use maps and set to dry antecedent moisture conditions (AMC I). KLEM is forced by the 10-min radar-derived QPEs from 22 to 24 September 00:00 UTC. The computational model time-step aligns with the 10-min radar observing frequency.

### 3.4 Socioeconomic information

Socioeconomic data regarding impacts is acquired from press news and payments disbursed by the Consorcio de Compensación de Seguros (CCS). The CSS is the Spanish entity responsible for compensating damages in case of natural hazards. Real-time monitoring of the early warning procedure is carried out by closely following the information issued by Civil Protection and the SMC via social networks. After the flash flood, a citizen campaign was developed to collect more



information (Llasat-Botija et al., 2022). The FLOOD-UP FRANCOLÍ campaign consisted of a participatory citizen science process conducted in collaboration with the Museum of Rural Life of the Espluga de Francolí. The primary objectives were: (i) to collect detailed information to facilitate the reconstruction of the episode; (ii) to identify the key impacts and adaptation behaviours and actions, and; (iii) to determine the level of understanding of the issued alerts and the most effective communication channels. The campaign was additionally designed to contribute improving citizens' preparedness for future episodes by promoting participation and fostering shared reflection on the first-hand experience.



## 4 Hydrometeorological factors

### 4.1 Mesoscale processes and role of orography

A control numerical simulation is designed to identify the key mesoscale ingredients simultaneous to the development of the HPE. Furthermore, a complementary non-orographic numerical simulation is performed to assess whether local and regional orography played a crucial role in the unfolding and stationarity of torrential rainfall.

A comprehensive set of mesoscale diagnostic products focusing on low levels is shown in Figs. 4 and 5 for two representative times, 15:00 and 21:00 UTC on 22 October. Except for the storm relative helicity field, which would rather apply to the examination of severe weather environments (e.g., squall line or supercell thunderstorm genesis), the rest of products emphasize the special characteristics of this HPE, regarding the triggering of the convective precipitation systems and their efficient feeding –during several hours– with moist, unstable Mediterranean air.

The surface wind fields confirm the impinging of a south-easterly flow towards the Catalanian pre-coastal orography (Figs. 4a and 5a). Such direction is optimal for the mechanical uplift of surface parcels by the mountain slopes of Tarragona, since its ridges are aligned parallel to the coastline (Romero et al., 1999). Broadly speaking, the impinging surface airflow is the leading portion of a maritime low-level jet (LLJ) pattern that initiates towards the south-western coasts of Sardinia. This LLJ tends to reinforce and shift northwards during the second half of 22 October, in association with the evolution of the synoptic-scale system described in section 2.2. An additional feature of interest that enhances the low-level convergence in the southern sector of Catalonia, where the convective systems developed and persisted several hours, is the north-westerly flow channelled along the Ebro valley, which encounters –in the opposing direction– the abovementioned maritime flow. Although



250 this feature losses entity during night (Figs. 1 and 5a), the combined pattern of land and maritime flows and the corresponding convergence over Tarragona and nearby sea persisted during the entire HPE.

The maritime flow against the coast maintains coherence through the low troposphere (see, for instance, the wind field at 850 hPa in Figs. 4 and 5). As expected, this airflow brings plenty of moisture of Mediterranean origin towards the Catalanian coast, as evidenced by the simulated values of vertically-integrated precipitable water above 40 mm. Since this  
255 pattern persisted during several hours, the atmospheric circulation clearly favoured a continuous feeding of the precipitation systems and its quasi-stationary character. That is, the so-called convective train effect: a successive development of convective cells in a line lying over the same zone (Doswell et al., 1996).

Two basic ingredients for the development and maintenance of deep moist convection were: the (i) low-level water vapour flux convergence, and; (ii) upward vertical motion. Both factors were synoptically-driven with a  
260 mesoscale/topographically forced motion. However, an additional ingredient became crucial for the development and maintenance of deep moist convection: ingestion of air parcels possessing convective or latent instability (e.g., Doswell et al., 1998; Romero et al., 2000). The model-simulated CAPE (Figs. 4c and 5c) during the most intense phase of the episode, confirms this important requirement of the synoptic/mesoscale environment: moderate to high values of CAPE existed on 22 October 2019 over the western Mediterranean Sea. These unstable vertical profiles were persistently advected towards the  
265 coastlands of Catalonia.

In summary, the control simulation is apparently successful in capturing both the synoptic and mesoscale processes/ingredients responsible for the onset, intensification, and maintenance of a slow-moving convective system over south-western Catalonia. As a result, the model effectively simulates extreme precipitation rates in this region from the afternoon of 22 October until early hours of next day (Figs. 4d and 5d). The same panels display the sea level pressure field  
270 during the convective event, highlighting the important role of the western Mediterranean cyclogenesis and the rather slow progression of the resulting low for the configuration of the abovementioned kinematic and thermodynamic ingredients.

Finally, it is repeatedly hypothesized that the topographically complex terrain of the affected area, and particularly the arrangement of the precoastal mountain ridges in Tarragona, basically parallel to the coast, would ultimately have been the critical element for the disproportionate rain totals and intensities over the Francolí catchment. This hypothesis is fully



275 confirmed when examining the results of a new simulation in which the terrain elevation is removed, while land/sea transition and the rest of surface characteristics are maintained. In particular, the total precipitation amount during the event yielded by this non-orographic simulation merely reaches 50 mm over the area of interest, in stark contrast with a maximum value above 300 mm in the control simulation (Fig. 6).

It should be noted that a general structure of heavy precipitation –oriented in the NW-SE direction and crossing the western half of Catalonia– is still found in this perturbed simulation, highlighting the flood potential of the described meteorological setting by itself. Local orography, however, emerges once again as the differential feature leading to catastrophic consequences, as in many other western Mediterranean past flash flood events (Gaume et al., 2004; Delrieu et al., 2005; Borga et al., 2007; Zanon et al., 2010; Amengual et al., 2007 and 2017).

#### 4.2 Precipitation analysis

285 According to the five automatic rain-gauge stations which recorded the highest rainfall amounts for the entire episode –varying from 240.4 mm to 299.5 mm– over the study region, three successive organized convective bands resulted in cumulative precipitation ranging from 50.3 mm to 72.3 mm between 02:00 and 14:00 UTC on 22 October (Fig. 7a). The maximum 10-min rainfall intensity varied between 28.5 mmh<sup>-1</sup> and 42.0 mmh<sup>-1</sup> during this period. Simultaneously with an hour rainfall hiatus inside the catchment, a persistent and elongated area of convection developed to the southwest and gradually moved north-eastward towards the basin.

From 16:00 to 20:00 UTC, the convective systems remained quasi-stationary over the western Francolí headwaters, leading to heavy rainfall that overwhelmed this area (Fig. 7b). The persistent convective systems resulted in bursts of rain, with a maximum 10-min rainfall rate of 124.8 mmh<sup>-1</sup> and a 4-h accumulation of 193.4 mm. According to the selected pluviometers, the duration of 10-min precipitation intensities exceeding 20 mmh<sup>-1</sup> ranged from 3.5 h to nearly 5 h, while the duration of 10-min rainfall rates above 50 mmh<sup>-1</sup> varied between 0.3 h and 1.5 h. From 21:00 UTC, a last organized convective band moved across the watershed from south to north, causing a third wave of precipitation that lasted approximately 5 h (Fig. 7c). Cumulative precipitation ranged from 29.8 mm to 39.5 mm among the selected rain-gauges, with maximum 10-min rainfall rates ranging between 18.0 mmh<sup>-1</sup> and 26.4 mmh<sup>-1</sup>.



The 48-h radar-derived rainfall field confirms that the lifting caused by local topographic forcing played a crucial role  
300 in amplifying the maximum rainfall amounts over the north-western headwaters of the Francolí catchment (Fig. 3).  
Precipitation amounts exceeding 150 mm were confined to this particular area, with cumulative rainfall surpassing 300 mm in  
the highest mountainous reliefs. This spatial concentration of total storm precipitation is evident in terms of the areas where a  
given amount of rainfall was exceeded. The extent of the areas surpassing the 200-mm and 300-mm thresholds was  
approximately of 110 km<sup>2</sup> and 25 km<sup>2</sup>, respectively.

305 The main features of this HPE over the Francolí watershed are investigated by analysing the 10-min catchment  
average rainfall rates and the proportion of the drainage area affected by 10-min rainfall rates exceeding 20 mmh<sup>-1</sup> and 50  
mmh<sup>-1</sup>. Both metrics are commonly used to describe rainfall conducive to flash flooding as they link the influence of rain and  
basin scales on hydrological response (Zhang et al., 2001; Smith et al., 2002; Borga et al., 2007; ten Veldhuis et al., 2018).  
Furthermore, the dependence between basin size and exceedance area above a specific set of rainfall amount thresholds,  
310 ranging from 25 mm to 400 mm, is investigated. Additionally, the relationship between the temporal and spatial scales of  
precipitation intensities surpassing 20 mmh<sup>-1</sup> and 50 mmh<sup>-1</sup> is explored (Fig. 8).

The catchment-area average total rainfall and maximum 10-min basin-area average precipitation rate were: 33.9 mm  
and 9.1 mmh<sup>-1</sup> from 02:00 to 14:00 UTC; 62.8 mm and 57.8 mmh<sup>-1</sup> from 16:00 to 20:00 UTC, and; 31.8 mm and 15.6 mmh<sup>-1</sup>  
from 20:00 UTC on 22 October to 02:00 UTC on 23 October. Interestingly enough, the exceedance drainage areas above the  
315 selected rain thresholds are connected by a strong logarithmic relationship ( $R^2=0.99$ ; Fig. 8c). This suggests that, at least for  
this case study, the spatial organization of total rainfall amount could have served as a useful predictive proxy for identifying  
basin scales that were most likely to experience runoff triggering.

A striking feature of this HPE is that 10% of the basin size experienced rainfall intensities larger than 20 mmh<sup>-1</sup> for  
more than 4 h, and precipitation rates higher than 50 mmh<sup>-1</sup> for 1 h (Fig. 8d). Furthermore, 5% of the total catchment area was  
320 subjected to precipitation rates of 20 mmh<sup>-1</sup> for almost 7 h, and 50 mmh<sup>-1</sup> for 2.5 h. It is worth noting that the spatial and  
temporal scales of these rainfall rates also exhibit a logarithmic decrease up to 100 km<sup>2</sup> for this case study. For larger scales,  
the time decrease exhibits a tail with drainage extent (Fig. 8d). This behaviour can be expected if heavy and persistent rain is  
the result of a certain hierarchical organization of convective system. Specifically, short-lasting and small-sized convective



cores with very high rainfall rates are embedded with more persistent convective clusters characterized by lower precipitation intensities, which, in turn, are embedded within even larger convective structures of even lower rainfall rates. If the hierarchical convective system organization is inverted, the spatial and temporal scales of deep and moist convective activity can result in a self-similar organization between maximum 30-min rainfall rates and total precipitation amounts over a region (Amengual, 2022). In the end, the hierarchy of a flash-flood producing storm is influenced by its spatial structure and temporal evolution, orographic enhancement and quasi-stationarity.

### 330 4.3 Flood response and water balance

#### 4.3.1 Basin response

According to radar estimates, the catchment-average total rainfall amount was 129.9 mm, while the runoff ratio over the entire basin was remarkably small, of 0.1 (Table 1). The severe soil moisture deficit in the Francolí catchment was a result of the long, warm and dry summer typical of the Mediterranean climate. September 2019 experienced above-average 335 temperatures and below-average rainfall, with total observed amounts within the basin being less than 35 mm. October was also warmer and drier than average, with maximum cumulative precipitation reaching only 20 mm until 20 October (SMC, 2019a and b).

From 02:00 to 14:00 UTC on 22 October, the rainfall rates and amounts were not large enough to result in infiltration-excess runoff generation. However, they did ameliorate the strong deficit in soil moisture content. The extreme precipitation 340 intensities and amounts between 16:00 and 20:00 UTC led to a paradigmatic case of fast infiltration-excess runoff generation. Specifically, from 18:50 to 19:40 UTC, the north-western Francolí basin suffered the most striking rainfall period, with a total catchment-area average precipitation of 34.3 mm and a maximum 10-min basin-area average rainfall rate of  $57.8 \text{ mmh}^{-1}$ . Furthermore, the maximum basin fraction covered by rainfall intensities greater than  $20/50 \text{ mmh}^{-1}$  was of 0.67/0.38, affecting drainage areas of  $574.0/322.6 \text{ km}^2$ , respectively (Figs. 8a and b). This very heavy rainfall burst, lasting for approximately an 345 hour, produced a flash flood with catastrophic impacts over drainage areas ca  $500 \text{ km}^2$ .

The availability of automatic stream-gauge data is limited to a site near the mouth of the Francolí river, in Tarragona (Table 1; Fig. 1). Unfortunately, the automatic flow station located in Montblanc, which closes the upper Francolí catchment, was damaged by the flood bore. Before its destruction, the stream gauge recorded a sudden and significant increase in flow



from  $2.3 \text{ m}^3\text{s}^{-1}$  at 20:10 UTC to  $186.2 \text{ m}^3\text{s}^{-1}$  at 20:15 UTC on 22 October. The Tarragona station observed a main peak discharge  
350 of  $871.0 \text{ m}^3\text{s}^{-1}$  at 22:30 UTC. Prior to this peak, a very minor peak of  $75.4 \text{ m}^3\text{s}^{-1}$  had been measured at 22:00 UTC. The rising  
limb of the hydrograph was exceptional steep, with discharge increasing from  $65.6 \text{ m}^3\text{s}^{-1}$  to  $871.0 \text{ m}^3\text{s}^{-1}$  in just 15 minutes (Fig.  
9). That is, the discharge multiplied by more than 13 times. Furthermore, the peak discharge was more than 2900 times the  
daily mean baseflow on 21 October, which was  $0.3 \text{ m}^3\text{s}^{-1}$ , highlighting the dominant contribution of fast superficial flow. In  
response to the last rainy period of precipitation, a secondary peak discharge of  $212.3 \text{ m}^3\text{s}^{-1}$  was registered on 23 October at  
355 03:15 UTC.

Shortly after the occurrence of the flash flood, Martín-Vide et al. (2023) conducted a comprehensive field campaign  
that involved post-flood field observations and interviews with local residents. Field work focused on documenting high  
watermarks and changes in channel geometry at various hydrometric sections along the upper Francolí watershed. Eyewitness  
accounts provided valuable information on the severity of the flood, the rates of stream rise, and the timing of peak discharges.  
360 Following hydraulic modelling, a range of plausible peak discharges values were estimated (Table 1). Variation in specific  
peak discharge with cumulative precipitation highlights the marked nonlinear nature of basin response. Furthermore, the abrupt  
changes in flood wave celerity along the Francolí river reveals significant heterogeneities in flow hydraulics. The extremely  
sharp increase in water velocity estimated between the towns of the Espluga de Francolí and Montblanc (hydrometric sections  
5 and 6 in Table 1, Fig. 1) was attributed to the impact of several bridges along this river section on the flood bore (for more  
365 detailed information, the reader is referred to Martín-Vide et al., 2023).

#### 4.3.2 Hydrological modelling

Hydrologic response is further examined by implementing the KLEM model. Calibration efforts are focused on peak  
discharge, time-to-peak and runoff volume at the Tarragona hydrometric section. These features are primarily influenced by  
infiltration and surface flow velocities. During calibration, curve numbers and infiltration storativities are kept invariant. The  
370 initial abstraction ratio is adjusted to 0.35 due to the exceptionally low initial soil moisture content, so as to correctly simulate  
the observed water balance. Channel flow velocity is determined from field estimations, while the hillslope flow velocity is  
also considered as a calibration parameter (Tables 1 and 2; Fig. 9).



The skill of QPEs-driven runoff simulation is assessed using the Nash–Sutcliffe efficiency criterion (NSE; Nash and Sutcliffe, 1970). The performance of the hydrological model is also evaluated by calculating the relative errors in peak discharge and total direct runoff volume, expressed as a percentage. After calibration, KLEM adequately captures the overall basin response, exhibiting a high goodness-of-fit in terms of peak magnitude and timing. However, the observed water balance is moderately overestimated at the expense of a slight underestimation in peak discharge (Table 3; Fig. 9). The adequate performance of the hydrological simulation can be partially attributed to the significant impact of the burst of heavy rainfall between 18:50–19:40 UTC, which strongly modulated basin response. As QPEs are estimated with relatively good accuracy over the Francolí basin, it is unlikely that inaccuracies in the simulated water balance emerge from large errors in QPEs (Fig. 3). Instead, these imprecisions are more likely due to errors in accurately representing soil response to heavy rainfall.

Errors in the simulated water balance primary stem from inaccuracies in reproducing the observed rising limb of the hydrograph, resulting in an excessive initial runoff volume (Fig. 9). The Francolí watershed exhibited a combination of high abstractions and subsequent extreme infiltration-excess runoff rates. The presence of these large soil retention capabilities is associated with the recharge of deep aquifers through infiltration, percolation and transmission losses along the river beds. This feature in catchment response has also been documented in other catastrophic flash floods (Smith et al., 1996; Martín-Vide et al., 1999; Camarasa-Belmonte and Beltrán Segura, 2001; Gaume et al., 2003; Delrieu et al., 2005; Borga et al., 2007; Zanon et al., 2010; Amengual et al., 2017; Amengual, 2022).

### 4.3.3 Sensitivity tests

Three sensitivity tests are devised to evaluate the influence of different factors on the unfolding of the flash flood. The first sensitivity test (labelled as *test 1*) focuses on the role of initial soil moisture content in hydrological response. In this simulation, only the rainfall that occurred from 16:00 UTC on 22 October onwards is considered, disregarding the previous precipitation during the event. Curve numbers are set to represent normal antecedent moisture conditions (AMC II), based on the SCS recommendation of 5-days total antecedent rainfall up to 53.3 mm for high evapotranspiration rates. The second sensitivity test (labelled as *test 2*) assesses the effect of the early precipitation between 02:00 and 14:00 UTC on 22 October, before the onset of the most intense rainfall period. In this experiment, the precipitation during this ~~time~~ period is also disregarded, while curve numbers remain the same as in the control simulation, representing AMC I.





The third sensitivity test (labelled as *test 3*) examines the role of the heaviest rainfall rates from 18:50 to 19:40 UTC on 22 October on basin response. In this experiment, the variability in 10-min rainfall during this temporal span is smoothed out by considering its temporal average. That is, instead of using the actual 10-min precipitation rates, a constant and averaged 10-minute rainfall intensity of  $33.9 \text{ mmh}^{-1}$  is employed for the entire 18:50–19:40 UTC period. Test 3 maintains the same curve numbers as in the control simulation and it preserves the total rainfall amount of the event. The remaining KLEM parameters are kept invariant through the sensitivity experiments to ensure consistency with the control simulation (Table 2; Fig. 9).

Firstly, results indicate significant overestimations of the simulated peak discharge and total runoff volume for test 1, even when the catchment average cumulative precipitation during the event is smaller (Table 4; Fig. 10). This outcome would indicate that soil moisture was far from saturation prior to the extreme precipitation intensities and amounts that triggered the 22 October 2019 flash flood. Secondly, test 2 suggests the importance of the early rainy period between 02:00 and 14:00 UTC on 22 October. This early precipitation stage was instrumental for the development of the catastrophic flash flood: it moistened the topsoil, resulting in decreased infiltration rates. As a result, it promoted large infiltration-excess runoff ratios as response to the subsequent extreme rainfall intensities and amounts. This finding would support the hypothesis that until runoff thresholds were exceeded, massive generation of infiltration-excess runoff was not triggered, in line with previous findings by Gaume et al. (2004), Borga et al. (2007) and Amengual (2022) when examining catastrophic flooding in the Western Mediterranean.

Finally, test 3 would indicate that the rainfall intensities between 18:50–19:40 UTC played a fundamental role in triggering sudden and large infiltration-excess runoff rates. Rainfall variability resulted in an enhanced and very narrow peak discharge, promoting a very flashy basin response (Table 4; Fig. 10). This flash flood was primarily the result of the combination of a high precipitation volume, alleviating the acute soil water deficit, and extreme rainfall intensities that overwhelmed soil infiltrability. These findings suggest that runoff triggering was intimately connected to the spatial and temporal variability of the convective precipitation. That is, the acute infiltration-excess runoff generation was relatively short-lived, as the recession limb of the flood decreased very fast after the peak discharge. In fact, it took just one hour for the flow to recede to 50% of the maximum peak, which corresponds to the temporal span of the heaviest rainfall period (Fig. 9). The



presence of a larger simulated than observed secondary maximum peak discharge in response to the last rainy period would suggest that losses persisted even after the onset of the catastrophic flash flood.

## 425 5 Catchment and social dynamics

### 5.1 Catchment response times

Field data and the control hydrological simulation support the observation that the Francolí basin experienced paroxysmal runoff and dynamic processes, characteristic of extreme flooding. According to the control simulation, the catchment average hillslope flow velocity was  $0.25 \text{ ms}^{-1}$ , while field estimates point out a channel averaged flow velocity of  
430  $4.5 \text{ ms}^{-1}$  (Tables 1 and 2). These high superficial flow velocities were primarily a result of the steep hillslopes and river beds in the upper catchment. In addition, several studies have indicated that during extreme flash flooding, large amounts of sheet flow generated on the hillslopes can concentrate in previously unchannelized areas, leading to increased water velocity (Smith et al., 2002; Borga et al., 2007). In this event, it seems that the extensive vegetation cover in the upper Francolí watershed contributed to slow down the overland flow by increasing surface roughness and providing resistance to flow. Previous studies  
435 examining similar extreme flash floods in mountainous catchments of Mediterranean Spain have estimated hillslope velocities comprised between  $0.35 \text{ ms}^{-1}$  and  $0.40 \text{ ms}^{-1}$  (Lorenzo-Lacruz et al., 2018; Amengual et al., 2022).

Undoubtedly, people responsible for risk management must cope with unusually short lead times when confronted with these sudden natural hazards in Mediterranean Spain. It is of the maximum interest to quantify the hydrological response times across drainage scales for the paradigmatic 22 October 2019 flash flood and to compare them with the timing of social  
440 response at different spatial scales. Comparing both response times could assist in developing more effective strategies for flood forecasting, early warning systems, and emergency response planning.

Catchment response time is influenced by drainage extent, runoff generation, and hillslope and channel network routing. Lag time is a useful measure to characterize basin dynamics, and it can be defined as the temporal difference between the centre of mass of the rainfall hyetograph and the timing of peak discharge (Creutin et al., 2009). Lag times are computed  
445 by using observations, post-flood field estimates and the hydrological control simulation. To provide a reference, the lag times for the 22 October 2019 event are compared to the power-law relationships established by Marchi et al. (2010) in their study



on flash flood features across Europe (Fig. 11). These authors empirically derived the following envelope curves, characterizing the lower limit of lag time,  $T_L$  (in h), versus basin area,  $A$  (in  $\text{km}^2$ ):

$$450 \quad T_L = \begin{cases} 0.08 \cdot A^{0.55} & \text{for } A \leq 350 \text{ km}^2 \\ 0.003 \cdot A^{1.10} & \text{for } A > 350 \text{ km}^2 \end{cases}$$

Lag times were less than 2 h for basin areas up to  $50 \text{ km}^2$ , of 2.5–3 h for drainage extents ranging from  $50 \text{ km}^2$  and  $350 \text{ km}^2$ , and of 3–3.5 h for catchment extensions between  $375\text{--}810 \text{ km}^2$  (Fig. 11). Interestingly, lag times feature a relative constant value of roughly 1.5 h for basin areas less than  $15 \text{ km}^2$ . Similarly, the response times remain relatively steady at about  
455 1.8 h for drainage extents between  $15 \text{ km}^2$  and  $40 \text{ km}^2$ . These outcomes suggest that these drainage areas experienced similar rainfall severity and duration, resulting in comparable times-to-peak. Another noteworthy observation is the contrasting impact of increasing drainage area on lag time. Basin extents larger than  $350 \text{ km}^2$  are near the lower limit of the envelope curve, while lag times for drainage areas smaller than  $350 \text{ km}^2$  are well above the lower envelope bound (Fig. 11).

This behaviour can be attributed to the relatively delayed basin response to precipitation at small drainage scales due  
460 to the large soil moisture replenishment and the effect of runoff threshold exceedance. The lower envelope limit of lag time for watersheds smaller than  $350 \text{ km}^2$  is determined by the occurrence of flash flooding in Continental Europe (Marchi et al., 2010). According to these authors, these natural hazards unfold during the prevalent regime of short-duration and low-amount rainfall events typically associated with summer storms and normal-to-wet soil initial conditions. Soils that are closer to saturation exhibit a faster response to precipitation than compared to very dry soils, resulting in shorter lag times at small  
465 scales. Nevertheless, mean residence time strongly relies on other ingredients: the distance between the catchment outlet and the geometrical centre of mass of the event runoff and the flow velocity (Woods and Sivalapan, 1999). The response times of the 22 October 2019 event for drainage sizes larger than  $350 \text{ km}^2$  were strongly influenced by the flow hydraulics. Particularly, the high channel velocities in some river sections led to a sharp transition in lag time with increasing drainage size. As a result, the lag times for catchments larger than  $350 \text{ km}^2$  lie on the lower limit of the envelope curve (Table 1; Fig. 11).



## 470 5.2 Social impacts and response times

### 5.2.1 Social response and aftermath

Creutin et al. (2009) categorized social response in three different types of actions: information, organization, and protection. The information step involves collecting data and ensuring its quality and relevance through comparison with other inputs and involving several stakeholders. This phase initializes the warning cycle and aims to protect inhabitants and material  
475 goods through situation assessment. The organization stage synthesizes and analyses the gathered information, and leads to the implementation of structured responses in the form of pre-established defence plans. This step sets the stage of the subsequent protection phase, which concludes the cycle. The protection stage involves the deployment of preventive safety measures.

For the case under study, the information stage started on October 21, in response to forecasts of heavy rain, strong wind and sea waves by the SMC. The regional meteorological office issued a warning, indicating a high probability of rainfall  
480 exceeding 100 mm in 24 hours, with certain areas expected to experience up to 200 mm, as well as intense rains of 20 mm within a 30-minute interval. The SMC assigned the alert colour code as orange for the majority of the coastal counties in Catalonia, encompassing an area exceeding 12000 km<sup>2</sup>. The pre-coastal administrative divisions were designated as yellow alert, covering a spatial extent slightly over 8600 km<sup>2</sup> (Table 5). The organizational step began around noon on the same day  
485 when civil protection activated the pre-alert phase of the Flood Management Plan of Catalonia (INUNCAT). During the pre-alert phase, civil protection notifies local and regional administrations, broadcasts informatory and advisory warnings through the media and social networks, and coordinates the emergency response teams. Civil protection shared a tweet emphasizing the following specific recommendations for individuals to take preventive actions: (i) drive primarily on main routes and highways; (ii) reduce speed and maintain safe distances, and; (iii) avoid crossing any rivers, streams or flooded areas.

On the afternoon of October 21, the social response entered the protection stage. The INUNCAT plan was upgraded  
490 to the alert level, which involves systematic and preventive actions taken by all the relevant local and regional administrations. During this phase, the SMC carries out an uninterrupted weather surveillance and a continuous communication is maintained with the municipal stakeholders to monitor stream flows, assess traffic conditions and inform the population. Accordingly, the SMC continuously updated the alerts on October 22 due to the forecast of a medium-to-high probability of rainfall surpassing 200 mm within a 24-h period. Early in the afternoon, the orange and red codes had expanded over Catalonia, spanning areas



495 above 13000 and 7500 km<sup>2</sup>, respectively. The yellow alert covered an extension ca 8200 km<sup>2</sup> (Fig. 12). The municipalities  
along the Francolí river (Garrigues, Conca de Barberà, Alt Camp and Tarragonès, listed from up to downstream, Fig. 1)  
maintained a low probability of exceeding 200 mm of rainfall within a 24-hour period. In fact, the Garrigues county remained  
under the yellow code throughout the day, while the other administrative divisions were under an orange alert code (Table 5;  
Fig. 12). Therefore, the institutional response in terms of the organization-protection-prevention cycle started approximately  
500 30 to 24 hours before the flow peak, in line with previous findings by Creutin et al. (2009).

The alert phase continues as long as the situation can be managed with the existing resources of the civil protection  
service, and the impact on the population is either non-existent or reduced. On October 22, at 21:30 UTC, INUNCAT entered  
the emergency phase in response to the serious incidents developing inside the Francolí catchment. The emergency stage  
involves several key actions, such as: (i) establishment of a central emergency committee; (ii) immediate mobilization of all  
505 relevant response teams and resources for rescue, evacuation and accommodation purposes; (iii) determination of the extent  
of flooding; (iv) extensive communication with the media to provide updates on the flood situation, meteorological conditions,  
road network status and alternative routes, and; (v) dissemination of information to the population, including instructions and  
recommendations for self-protection. The emergency phase continued during the morning of October 23 over the counties  
crossed by the Francolí river, due to the significant impacts that had been experienced (Fig. 12).

510 The overall episode caused 7 fatalities in Catalonia, 6 of which occurred inside the Francolí basin. The flash flood  
affected numerous riverside towns such as Vimbodí, Poblet, Montblanc and Vilaverd. Impacts were primarily due to the  
forceful flow of water carrying solid debris. One of the most affected municipalities was the Espluga de Francolí. Some  
riverside buildings such as a wine cellar and a restaurant were completely destroyed. Fortunately, both establishments were  
unoccupied and closed to the public at the time of their destruction. Additionally, numerous residences, roads, bridges, railways  
515 and other infrastructure suffered extensive damage. Flooding also affected lowlands, cultivated fields and the local  
manufacturing, especially the agrifood industry due to the destruction of crops and the loss of livestock. The CCS paid a total  
compensation of 44 million euros for the insured damages across Catalonia.

According to the insights from the FLOOD-UP FRANCOLÍ campaign, residents remembered that the most  
devastating period of destruction took place between 19:30 and 22:00 UTC on 22 October. This perception was attributed to



520 the force of the water and the obstruction of the bridge's arch caused by the woody debris carried by the flood in the Espluga de Francolí. In this riverside town, a car carrying two elderly men and a driver along with his truck were swept away by the raging waters on this bridge. This incident took place between 20:00 and 20:30 UTC, resulting in the loss of all three occupants' lives. In Vilaverd, a bungalow was drifted, killing the two inhabitants around 21:00 UTC (Fig. 12). The sixth casualty was found in the Pobla de Mafumet (basin extent ca 750 km<sup>2</sup>), a location further downstream from the drainage areas that  
525 experienced the most catastrophic consequences. The precise location and timing of this victim being swept away by the flood bore remain unknown.

### 5.2.2 Citizen perception

The citizen campaign has also allowed to evaluate the follow-up of the warning system. According to the eyewitnesses, the peak of precipitation occurred on October 22 between 18:00 and 20:00 UTC. More than half of the  
530 respondents received the warning, with television being the most frequently mentioned media, followed by the City Council and social networks (including the Civil Protection and SMC accounts). All respondents reported an easy understanding of the warnings. Regarding the recommendations they received, most participants remembered being advised to avoid proximity to rivers and displacements. In general, they felt very well informed, although 33% of respondents indicated feeling uninformed. When asked about their understanding of the probability classification and warnings provided by the SMC (Table 5), 60%  
535 expressed a lack of comprehension. While over half of the participants considered the episode as exceptional, stating that "they had never witnessed such severe floods before", a significant majority (66%) did not perceive any threat to their homes or properties. Furthermore, none of the participants reported feeling endangered in terms of their personal safety. These personal impressions align with previous findings by Creutin et al. (2009), who stated that rising water levels in rivers are the primary trigger for individual and community organization and protection actions on scales smaller than 100 km<sup>2</sup>, rather than the  
540 information provided by public administrations. Institutional actions tend to apply at administrative scales ca 800 km<sup>2</sup> in average over Catalonia.



## 6 Conclusions

The analysis of the hydrometeorological factors, catchment dynamics, and social actions ~~has~~ unravelled the main ingredients that concurred in the catastrophic consequences of the 22 October 2019 flash flood. The synoptic situation was dominated by a nearly stationary upper-level cold cut-off located over southern Spain. The formation of a slow-moving surface cyclone led to a set of key mesoscale ingredients that promoted the formation of a convective train. In particular, the persistent impinging of a south-easterly Mediterranean flow advected warm and moist air towards the Catalanian pre-coastal topography. Local orography played a paramount role in organizing the mesoscale flow over Catalonia and acted as a convection-triggering mechanism. The continuous latent heat flux from the Mediterranean Sea moistened the low troposphere, enhancing convective instability and increasing rainfall efficiency.

Extreme precipitation was concentrated upon the north-western mountain ridges of the upper Francolí basin. According to the QPEs, rainfall values in excess of 200 mm impacted a limited spatial extent ~~ca~~ 100 km<sup>2</sup>. Interestingly enough, the exceedance drainage areas above a selected set of precipitation thresholds exhibited a robust logarithmic relationship for this particular episode. The spatial scales of rainfall organization would have been a valuable predictive proxy for those drainage scales most likely to experience sudden infiltration-excess runoff generation. This behaviour was also observed for 10-min rainfall rates exceeding 20/50 mmh<sup>-1</sup> over drainage scales smaller than 100 km<sup>2</sup>.

The sensitivity ~~hydrological~~ tests provided some insights about the relative roles of different factors on the onset of this catastrophic flash flood. The very dry initial soil conditions strongly modulated catchment response, dampening flood peak and runoff volume with respect to rainfall amount. That is, the large soil moisture deficit promoted a marked non-linearity in basin response to precipitation rates and amounts. Antecedent precipitation prior to the most intense rainfall period was also instrumental: Although it did not produce runoff, it moistened the topsoil and reduced infiltration rates, favouring the exceedance of runoff thresholds. The subsequent extreme precipitation intensities and amounts triggered acute infiltration-excess runoff rates: Rainfall variability modulated the very flashy and short-lived extreme basin response.

The relative delay in runoff triggering resulted in hydrological responses comparatively long for basin scales up to 100 km<sup>2</sup>. Effectively, lag times were well above the envelope curve characterizing the minimum lag times typically observed for flash floods in Europe. This threshold-type hydrological behaviour led to a belatedly, but then sudden and massive runoff



production. The subsequent flood bore routed very fast, while carrying a large amount of woody and vegetation debris. The debris interaction with several bridges along the river caused significant heterogeneities in flow hydraulics. As consequence, a stark transition in lag time occurred for basin scales larger than 350 km<sup>2</sup>, lying on the lower bound of the envelope curve.

570 Contrary to reports from other similar episodes in the Western Mediterranean region, most of fatalities occurred in relatively large drainage scales, ranging from 50 km<sup>2</sup> to 400 km<sup>2</sup>. Extreme rainfall rates and amounts were spatially limited, mainly affecting a densely forested and relatively inhabited mountainous area. The institutional organization-protection-prevention cycle developed at the spatial and temporal scales typically dominated by the meteorological factors. That is, the SMC issued a warning of risk for the occurrence of heavy rainfall at county scale up to 30 hours in advance to the occurrence  
575 of the tragic flash-flood. Simultaneously, civil protection activated the INUNCAT plan, while issuing a warning containing a set of recommendations for the population. Continuous updates to the warnings and the municipalities at very high danger of heavy rainfall were disseminated through traditional media channels and social networks.

A citizen science campaign was conducted to estimate social perception. The warnings issued by the SMC and civil protection were successful in reaching a significant portion of the population. The primary recommendations that interviewees  
580 recalled were to avoid displacements and to stay away from rivers. However, a third of the respondents did not feel adequately informed, and over a half of them were unfamiliar with the meaning of the different warning levels. Additionally, two-thirds of the participants did not perceive any threat to their homes, premises or properties, and none of them felt their lives were at risk. Considering the severe aftermath of the flash flood, this information corroborates the need for the population to improve their perception of the level of risk they may face.

585 The catastrophic effects distributed over a spatial extent ca 500 km<sup>2</sup> and a temporal scale of less than 3 h. To anticipate more effectively social responses at the spatial and temporal scales of the hydrological processes, the forecasting process should rely on hydrologic and hydraulic models driven by high-resolution reliable rainfall fields. However, errors in the initial and boundary atmospheric conditions, uncertainties in mesoscale model parameterizations and the complex and nonlinear nature of the processes involved in developing deep moist convection hinder the precise forecasting in location, intensity and  
590 timing of quasi-stationary HPEs triggering flash floods. In addition, small-scale extreme weather phenomena that initiate over the sea typically have significantly lower numerical predictability. Despite these challenges, three out of the four municipalities





crossed by the Francolí river were under a high risk alert before 15:00 UTC on 22 October. The remaining administrative unit was classified under moderate danger.

Given the inherent limitations in predicting storm-scale features, operational forecasting strategies can benefit from the use of short-range, convection-permitting ensemble prediction systems. These systems combined with real-time data assimilation techniques and hydrological modelling may provide additional guidance in anticipating flash flood situations over the Spanish Mediterranean region. The use of advanced hydrometeorological ensemble prediction systems can be complemented by real-time and reliable QPEs driven hydrologic-hydraulic forecasts. Furthermore, the relatively delay in runoff generation might provide an opportunity to expand the automatic observational networks to small basin scales. By incorporating real-time observations from rain- and stream-gauges located in the headwaters of mountainous catchments, it could become possible to enhance pre-existing alert systems and improve early warning capabilities. For instance, sound alarms could be installed along the river valley towns and integrated in the alert systems. These alarms could be activated in basis of monitoring predetermined rainfall threshold exceedance and sudden increases in discharge. The blending of all these approaches could provide civil protection with additional tools to implement anticipatory measures on the spatial and temporal scales over which flash floods develop.

It seems also urgent to revise urban planning and the management of flood-prone areas, as well as to enhance social awareness of the danger associated with flash flooding. The population may be educated on how to interpret probabilistic alerts and understand the inherent scales and uncertainties related to weather forecasting. Furthermore, it might become essential to provide further guidance on how to act appropriately when facing different kinds of natural hazards. Initiatives such as awareness campaigns could be carried out in schools, in between prime-time radio and television programs, and by involving media influencers on various social networks. In addition, text messages could be sent to mobile phones in areas on alert, informing the population about the dangerous weather situation and providing recommendations to follow. All these efforts could help individuals to make informed decisions and take necessary actions to protect themselves from natural hazards.



615 **Data availability**

The primary data used in this study (rain-gauge, stream-gauge and weather radar data) can be obtained under request to the Catalan Water Agency, the Catalan Meteorological Service and the Spanish Agency of Meteorology.

**Author contribution**

620 AA, RR and MCL designed the research. AA drafted the paper. AA, RR, MCL, AH and MLB performed the formal analysis and wrote, edited and revised the paper. AA, RR and AH elaborated the figures.

**Competing interests**

The authors have the following competing interests: At least one of the (co-)authors is a member of the editorial board of Natural Hazards and Earth System Sciences.

625

**Acknowledgements**

This work has been sponsored by the Ministerio de Ciencia e Innovación - Agencia Estatal de Investigación through the TRAMPAS (PID2020-113036RB-I00/AEI/10.13039/501100011033) and C3RiskMed (PID2020-113638RB-C22/MICIN-AEI/10.13039/501100011033) research projects. The authors are grateful to AEMET, especially to Ramón Pascual and  
630 Gabriela Cuevas, for providing technical documentation and different meteorological observations related to this flash flood event. The authors are also grateful to Eduard Marion from Meteoprades for supplying rainfall observations. The ACA and SMC agencies are acknowledged for providing other necessary data for conducting this research. The citizen campaign was supported by the AGORA project, funded by the ACA of Generalitat de Catalunya, and with the strong support of the Museu de la Vida Rural de l'Espluga de Francolí.

635



## 640 References

- Amengual, A., R. Romero, M. Gómez, A. Martín, and S. Alonso: A hydrometeorological modeling study of a flash-flood event over Catalonia, Spain. *J. Hydrometeorol.*, 8(3), 282-303, 2007.
- Amengual, A., Homar, V., and Jaume, O.: Potential of a probabilistic hydrometeorological forecasting approach for the 28 September 2012 extreme flash flood in Murcia, Spain. *Atmos. Res.*, 166, 10-23, 2015.
- 645 Amengual, A., Carrió, D. S., Ravazzani, G., and Homar, V.: A comparison of ensemble strategies for flash flood forecasting: The 12 October 2007 case study in Valencia, Spain. *J. Hydrometeorol.*, 18(4), 1143-1166, 2017.
- Amengual, A.: Hydrometeorological analysis of the 12 and 13 September 2019 widespread flash flooding in eastern Spain. *Nat. Haz. Earth Syst. Sci.*, 22(4), 1159-1179, 2022.
- Barettino, D. and Pujadas, J.: Programa I+D en Geología Ambiental. Estudio de avenidas en la cuenca alta del río Francolí (Tarragona). Mapas de peligrosidad por inundación. ITGE and Servei Geològic de Catalunya, 74 pp., ISBN: 978-84-7840-770-5, 1992.
- 650 Borga, M., P. Boscolo, F. Zanon, and M. Sangati: Hydrometeorological analysis of the 29 August 2003 flash flood in the Eastern Italian Alps. *J. Hydrometeorol.*, 8, 1049–1067, <https://doi.org/10.1175/JHM593.1>, 2007.
- Bouilloud, L., B. Delrieu, B. Boudevillain, M. Borga, and F. Zanon: Radar rainfall estimation for the post-event analysis of a Slovenian flash-flood case: Application of the Mountain Reference Technique at C-band frequency. *Hydrol. Earth Syst. Sci.*, 13, 1349–1360, <https://doi.org/10.5194/hess-13-1349-2009>, 2009.
- 655 Camarasa-Belmonte, A. M., and Beltrán Segura, F.: Flood events in Mediterranean ephemeral streams (ramblas) in Valencia region, Spain. *Catena*, 45, 229–249, doi:10.1016/S0341-8162(01)00146-1, 2001.
- Cloke, H. L. and Pappenberger, F.: Ensemble flood forecasting: A review. *Journal of hydrology*, 375(3-4), 613-626, 2009.
- 660 Cole, S., and R. Moore: Hydrological modelling using rain-gauge and radar-based estimators of areal rainfall. *J. Hydrol.*, 358, 159–181, <https://doi.org/10.1016/j.jhydrol.2008.05.025>, 2008.
- Cramer, W., Guiot, J., Fader, M., Garrabou, J., Gattuso, J.-P., Iglesias, A., Lange, M.A., Lionello, P., Llasat, M.C., Paz, S., Peñuelas, J., Snoussi, M., Toreti, A., Tsimplis, M.N., and Xoplaki, E.: Climate change and interconnected risks to sustainable development in the Mediterranean. *Nature Climate Change* 8:972-980, doi: 10.1038/s41558-018-0299-2, 2018.



- 665 Creutin, J. D., Borga, M., Lutoff, C., Scolobig, A., Ruin, I., and Créton-Cazanave, L.: Catchment dynamics and social response during flash floods: the potential of radar rainfall monitoring for warning procedures. *Meteor. Applications*, 16(1), 115-125, 2009
- Da Ros, D. and Borga, M.: Use of digital elevation model data for the derivation of the geomorphological instantaneous unit hydrograph, *Hydrol. Process.*, 11, 13–33, [https://doi.org/10.1002/\(SICI\)1099-1085\(199701\)11:1<13::AID-HYP400>3.0.CO;2-M](https://doi.org/10.1002/(SICI)1099-1085(199701)11:1<13::AID-HYP400>3.0.CO;2-M), 1997.
- 670 Delrieu, G. and coauthors: The catastrophic flash-flood event of 8–9 September 2002 in the Gard Region, France: a first case study for the Cévennes–Vivarais Mediterranean Hydrometeorological Observatory. *J. Hydrometeor.*, 6(1), 34-52, 2005.
- Doswell III, C. A., Brooks H., and Maddox, R.: Flash flood forecasting: An ingredient-based methodology. *Wea. Forecasting*, 11, 560–581, 1996.
- 675 Doswell III, C. A., C. Ramis, R. Romero, and S. Alonso: A diagnostic study of three heavy precipitation episodes in the western Mediterranean region. *Wea. Forecasting*, 13, 102-124, 1998.
- Diffenbaugh, N. S., and Giorgi, F.: Climate change hotspots in the CMIP5 global climate model ensemble. *Climatic Change*, 114(3–4), 813–822, <https://doi.org/10.1007/s10584-012-0570-x>, 2012
- Dudhia, J.: A non-hydrostatic version of the Penn State/NCAR mesoscale model: validation tests and simulation of an Atlantic cyclone and cold front. *Mon. Weather Rev.*, 121, 1493–1513, 1993.
- 680 Fulton, R., Breidenbach J., Seo D., Miller D., and O’Bannon T.: The WSR-88D rainfall algorithm. *Wea. Forecasting*, 13, 377–395, [https://doi.org/10.1175/1520-0434\(1998\)013,0377:TWRA.2.0.CO;2](https://doi.org/10.1175/1520-0434(1998)013<0377:TWRA.2.0.CO;2), 1998.
- Gaume, E., Livet, M., Desbordes, M., and Villeneuve, J. P.: Hydrological analysis of the river Aude, France, flash flood on 12 and 13 November 1999. *J. Hydrol.*, 286(1-4), 135-154, 2004
- 685 García-Herrera, R., Barropedro, D., Hernández, E., Paredes, D., Correoso, J. F., and Prieto, L.: The 2001 mesoscale convective systems over iberia and the Balearic Islands. *Meteor. and Atmos. Physics*, 90, 225–243, doi:10.1007/s00703-005-0114-2, 2005.
- Giannoni, F., Smith, J. A., Zhang, Y., and Roth, G.: Hydrologic modeling of extreme floods using radar rainfall estimates, *Adv. Water Resour.*, 26, 195–203, [https://doi.org/10.1016/S0309-1708\(02\)00091-X](https://doi.org/10.1016/S0309-1708(02)00091-X), 2003.



- 690 Gochis, D., and Coauthors: The great Colorado flood of September 2013. *Bull. Amer. Meteor. Soc.*, 96, 1461–1487,  
<https://doi.org/10.1175/BAMS-D-13-00241.1>, 2015.
- Grell, G., J. Dudhia and D. R. Stauffer: A description of the fifth-generation of the Penn State/NCAR mesoscale model (MM5).  
NCAR Tech. NCAR/TN-398+STR, 1995.
- Hapuarachchi, H. A. P., Wang, Q. J., and Pagano, T. C.: A review of advances in flash flood forecasting. *Hydrol. processes*,  
695 25(18), 2771–2784, 2011.
- Hermoso, A., Homar, V., and Amengual, A.: The sequence of heavy precipitation and flash flooding of 12 and 13 September  
2019 in eastern Spain. Part I: Mesoscale diagnostic and sensitivity analysis of precipitation. *J. Hydrometeorol.*, 22(5), 1117–  
1138, 2021.
- Hunter, S.: WSR-88D radar rainfall estimation: Capabilities, limitations and potential improvements. *Natl. Wea. Dig.*, 20, 26–  
700 36, 1996
- Leveque, R. J.: *Finite volume methods for hyperbolic problems*. Ed. Cambridge University Press, 558 pp., 2002
- Llasat, M. D. C., Rigo, T., and Barriendos, M.: The ‘Montserrat-2000’ flash-flood event: a comparison with the floods that  
have occurred in the northeastern Iberian Peninsula since the 14th century. *Int. J. Climatol.*, 23(4), 453–469, 2003
- Llasat, M.C., Llasat-Botija, M., Prat, M.A., Porcú, F., Price, C., Mugnai, A., Lagouvardos, K., Kotroni, V., Katsanos, D.,  
705 Michaelides, S., Yair, S., Savvidou, K., Nicolaidis, K.: High impact floods and flash floods in Mediterranean countries: the  
flash preliminary database. *Adv. Geosci.* 23, 1–9, 2010.
- Llasat-Botija, M., M.C. Llasat, S. Ruiz Navarro, C. Fernández Lopez: FLOOD-UP FRANCOLÍ. Retorn d’ experiència  
col·lectiu de les inundacions d’ octubre de 2019. VI Jornades sobre el Bosc de Poblet i Muntanyes de Prades, 2022.
- Lorenzo-Lacruz, J., Amengual, A., Garcia, C., Morán-Tejeda, E., Homar, V., Maimó-Far, A., Hermoso, A., Ramis, C., and  
710 Romero, R.: Hydrometeorological reconstruction and geomorphological impact assessment of the October 2018 catastrophic  
flash flood at Sant Llorenç, Mallorca (Spain). *Nat. Haz. Earth Syst. Sci.*, 19(11), 2597–2617, 2019
- Marchi, L., Borga, M., Preciso, E., and Gaume, E.: Characterisation of selected extreme flash floods in Europe and implications  
for flood risk management. *J. Hydrol.*, 394(1–2), 118–133, 2010.



- Martín, A., Romero, R., De Luque, A., Alonso, S., Rigo, T., and Llasat, M. C.: Sensitivities of a flash flood event over  
715 Catalonia: a numerical analysis. *Mon. wea. Rev.*, 135(2), 651–669, 2007.
- Martín-Vide, J. P., D. Nierola, A. Bateman, A. Navarro, and E. Velasco: Runoff and sediment transport in a torrential  
ephemeral stream of the Mediterranean coast. *J. Hydrol.*, 225, 118–129, 1999
- Martín-Vide, J. P., Bateman, A., Berenguer, M. Ferrer-Boix, C., Amengual, A., Campillo, M., Corral, C., Llasat, M. C., Llasat-  
720 Botija, M., Gómez, S., Marín-Esteve, B., Prats-Puntí, A., Ruiz-Carulla, R., Sosa-Pérez, R.: A flash flood with large woody  
debris clogged bridges. The 2019 event of Francolí River (NE Iberian Peninsula), *J. Hydrol.: Regional Studies*, 47, 101348,  
2023.
- Moore, R. J., and Bell, V. A.: Incorporation of groundwater losses and well level data in rainfall-runoff models illustrated  
using the PDM, *Hydrol. Earth Syst. Sci.*, 6, 25–38, <https://doi.org/10.5194/hess-6-25-2002>, 2002.
- Nash J.E. and Sutcliffe J.V.: River flow forecasting through conceptual models. Part I: A discussion of principles. *J. Hydrol.*  
725 10(3): 282–290, 1970.
- Paeth, H., Vogt, G., Paxian, A., Hertig, E., Seubert, S., and Jacobeit, J.: Quantifying the evidence of climate change in the light  
of uncertainty exemplified by the Mediterranean hot spot region. *Global and Planetary Change*, 151, 144–151,  
<https://doi.org/10.1016/j.gloplacha.2016.03.003>, 2017.
- Pastor, F., Gómez, I., and Estrela, M.: Numerical study of the October 2007 flash flood in the Valencia region (Eastern Spain):  
730 The role of orography. *Nat. Hazards and Earth Sys. Sci.*, 10, 1331–1345, doi:10.5194/nhess-10-1331-2010, 2010.
- Pellarin, T., G. Delrieu, G. Saulnier, H. Andrieu, B. Vignal, and J. Creutin: Hydrologic visibility of weather radar systems  
operating in mountainous regions: Case study for the Ardèche Catchment (France). *J. Hydrometeor.*, 3, 539–555,  
[https://doi.org/10.1175/1525-7541\(2002\)003<0539:HVOWRS.2.0.CO;2](https://doi.org/10.1175/1525-7541(2002)003<0539:HVOWRS.2.0.CO;2), 2002.
- Postigo, C., de Alda, M. J. L., Barceló, D., Ginebreda, A., Garrido, T., and Fraile, J.: Analysis and occurrence of selected  
735 medium to highly polar pesticides in groundwater of Catalonia (NE Spain): An approach based on on-line solid phase  
extraction–liquid chromatography–electrospray–tandem mass spectrometry detection. *J. Hydrol.*, 383(1–2), 83–92, 2010.
- Pujadas, J.: Mapa de riscos d'inundació i riscos associats a la Riba, Riu Francolí. *Cartografia de Riscos d'Inundació, Campanya*  
1994, <http://hdl.handle.net/2445/170580>, 1994.



- Roca, M., Martín-Vide, J.P., Moreta, P.J.M. Modelling a torrential event in a river confluence. *J. Hydrol.*, 364, 207-215, 2009.
- 740 Romero, R., G. Sumner, C. Ramis, and A. Genovés: A classification of the atmospheric circulation patterns producing significant daily rainfall in the Spanish Mediterranean area. *Int. J. Climatol.*, **19**, 765-785, 1999.
- Romero, R., C. A. Doswell III, and C. Ramis: Mesoscale numerical study of two cases of long-lived quasistationary convective systems over eastern Spain. *Mon. Wea. Rev.*, **128**, 3731-3751, 2000.
- Romero, R., M. Vich, and C. Ramis: A pragmatic approach for the numerical prediction of meteotsunamis in Ciutadella  
745 harbour (Balearic Islands). *Ocean Modelling*, DOI 10.1016/j.ocemod.2019.101441, 2019.
- Romero, R.: TRAM: A new nonhydrostatic fully compressible numerical model suited for all kinds of regional atmospheric predictions. *Quart. J. R. Meteorol. Soc.*, 2023, (submitted).
- Sendròs, A., Diaz, Y., Himi, M., Tapias, J. C., Rivero, L., Font, X., and Casas, A.: An evaluation of aquifer vulnerability in two nitrate sensitive areas of Catalonia (NE Spain) based on electrical resistivity methods. *Environ. earth sci.*, 71(1), 77-84,  
750 2014.
- Servei Meteorològic de Catalunya (SMC): Butlletí climàtic mensual. Setembre del 2019, 41 pp. Departament de Territori i Sostenibilitat, Generalitat de Catalunya, Barcelona, 2019a.
- Servei Meteorològic de Catalunya (SMC): Butlletí climàtic mensual. Octubre del 2019, 41 pp. Departament de Territori i Sostenibilitat, Generalitat de Catalunya, Barcelona, 2019b.
- 755 Smith, J. A., Baeck, M. L., Steiner, M., and Miller, A. J.: Catastrophic rainfall from an up-slope thunderstorm in the central Appalachians: The Rapidan storm of June 27, 1995. *Water Res. Res.*, 32(10), 3099-3113, 1996.
- Smith, J. A., M. L. Baeck, J. E. Morrison, and P. Sturdevant-Rees, D. F. Turner-Gillespie, and P. D. Bates: The regional hydrology of extreme floods in an urbanizing drainage basin. *J. Hydrometeor.*, 3, 267–282, [https://doi.org/10.1175/1525-7541\(2002\)003,0267:TRHOEF.2.0.CO;2](https://doi.org/10.1175/1525-7541(2002)003,0267:TRHOEF.2.0.CO;2), 2002.
- 760 ten Veldhuis, M.-C., Z. Zhou, Y. Long, S. Liu, and J. Smith: The role of storm scale, position and movement in controlling urban flood response. *Hydrol. Earth Syst. Sci.*, 22, 417–436, 2018, <https://doi.org/10.5194/hess-22-417-2018>.
- Tuel, A., and Eltahir, E. A.: Why is the Mediterranean a climate change hot spot? *Journal of Climate*, 33(14), 5829–5843 <https://doi.org/10.1175/JCLI-D-19-0910.1>, 2020.



USDA: Urban hydrology for small watersheds. USDA TR-55, 164 pp., 1986

765 Wicker, L. J., and W. C. Skamarock: A time-splitting scheme for the elastic equations incorporating second-order Runge-Kutta time differencing. *Mon Wea. Rev.*, 126, 1992-1999, 1998.

Woods, R.A. and Sivapalan, M.. A synthesis of space–time variability in storm response: rainfall, runoff generation and routing. *Water Resour. Res.* 35 (8), 2469–2485, 1999.

Wu, W., Emerton, R., Duan, Q., Wood, A. W., Wetterhall, F., Robertson, D. E.: Ensemble flood forecasting: Current status  
770 and future opportunities. *Wiley Interdisciplinary Reviews: Water*, 7(3), e1432, 2020.

Zanon, F., Borga, M., Zoccatelli, D., Marchi, L., Gaume, E., Bonnifait, L., and Delrieu, G.: Hydrological analysis of a flash flood across a climatic and geologic gradient: The September 18, 2007 event in Western Slovenia. *J. Hydrol.*, 394(1-2), 182-197, 2010.

Zhang, Y., J. A. Smith, and M. L. Baeck: The hydrology and hydrometeorology of extreme floods in the Great Plains of eastern  
775 Nebraska. *Adv. Water Resour.*, 24, 1037–1050, 2001.

780

785

790





795

## TABLES

| Hydrometric section  | Area (km <sup>2</sup> ) | Total rainfall (mm) | Total runoff (mm) | Peak discharge (m <sup>3</sup> s <sup>-1</sup> ) | Specific peak discharge (m <sup>3</sup> s <sup>-1</sup> km <sup>-2</sup> ) | Runoff ratio (-) | V <sub>c</sub> (ms <sup>-1</sup> ) | Time to peak (UTC) | Lag time (h) |
|----------------------|-------------------------|---------------------|-------------------|--|--|------------------|------------------------------------|--------------------|--------------|
| 1-Viern (headwaters) | 7.1                     | 370.3               | –                 | 40–110*  | 5.6–15.5   | –                | –                                  | –                  | –            |
| 2-Viern              | 9.5                     | 380.4               | –                 | 60–120*  | 6.3–12.6   | –                | –                                  | –                  | –            |
| 3-Milans             | 26.6                    | 341.2               | –                 | 115–360*   | 4.3–13.5   | –                | –                                  | 19:30*             | 1.8          |
| 4-Sec                | 38.8                    | 224.6               | –                 | 90–110*  | 2.3–2.8  | –                | –                                  | –                  | –            |
| 5-Espluga            | 99.5                    | 267.7               | –                 | 500–775*   | 5.0–7.8  | –                | 3.8–4.5*                           | 19:50–20:15*       | 2.2–2.6      |
| 6-Montblanc          | 339.9                   | 143.6               | –                 | 610–790*   | 2.0–2.3  | –                | 10.2*                              | 20:20–20:45*       | 1.7–2.1      |
| 7-Riba               | 449.0                   | 151.5               | –                 | 740–870*   | 1.6–1.9  | –                | 3.5*                               | 21:00–21:30*       | 2.5–3.0      |
| 8-Tarragona          | 809.1                   | 129.9               | 12.4              | 871.0  | 1.1  | 0.1              | 3.5*                               | 22:30              | 3.5          |

800 **Table 1** Main hydrometeorological features of the 22 October 2019 flash flood at the surveyed hydrometric sections. The total rainfall amount is derived from radar data and represents the area average value enclosed by each hydrometric section (see Fig. 1 for the locations). The times-to-peak correspond to October 22nd. Data marked with an asterisk (\*) denote estimations based on field observations and hydraulic modelling conducted by Martín-Vide et al., 2023.

805

| Basin    | Gauge     | CN (AMC I)  | I <sub>a</sub> (mm) | S (mm)        | V <sub>h</sub> (ms <sup>-1</sup> ) | V <sub>c</sub> (ms <sup>-1</sup> ) |
|----------|-----------|-------------|---------------------|---------------|------------------------------------|------------------------------------|
| Francolí | Tarragona | 44.9 (11.6) | 125.6 (66.7)        | 358.9 (190.5) | 0.25                               | 4.5                                |

810 **Table 2** KLEM parameters for infiltration and dynamical processes at the Tarragona hydrometric section. Curve numbers, initial abstractions and soil retention capacities are expressed as area-averaged values, while their standard deviations are shown in brackets.



815

| Basin    | Gauge     | Flow volume      |              |              | Flow peak                                     |   |              | NSE |
|----------|-----------|------------------|--------------|--------------|---|---|--------------|-----|
|          |           | Observed<br>(mm) | KLEM<br>(mm) | Error<br>(%) | Observed<br>(m <sup>3</sup> s <sup>-1</sup> ) | KLEM<br>(m <sup>3</sup> s <sup>-1</sup> ) | Error<br>(%) |     |
| Francolí | Tarragona | 12.4             | 15.1         | 21.5         | 871.0   | 798.8                                     | -10.9        | 0.7 |

**Table 3** Observed and radar-driven simulated flow volume and peak discharge at the Tarragona hydrometric section. Model performance also shown in terms of the different skill scores. Negative values in relative errors denote model underestimation.

820

| Experiment | Total<br>rainfall<br>(mm) | Flow volume      |              |              | Flow peak                                     |   |              | Time to<br>peak<br>(UTC) |
|------------|---------------------------|------------------|--------------|--------------|---|---|--------------|--------------------------|
|            |                           | Observed<br>(mm) | KLEM<br>(mm) | Error<br>(%) | Observed<br>(m <sup>3</sup> s <sup>-1</sup> ) | KLEM<br>(m <sup>3</sup> s <sup>-1</sup> ) | Error<br>(%) | KLEM                     |
| Control    | 129.9                     | 12.4             | 15.1         | 21.5         | 871.0   | 798.8                                     | -10.9        | 22:40                    |
| Test 1     | 95.9                      | 12.4             | 23.8         | 91.7         | 871.0   | 1171.5                                    | 32.0         | 22:40                    |
| Test 2     | 95.9                      | 12.4             | 6.8          | -45.4        | 871.0   | 315.7                                     | -64.0        | 22:40                    |
| Test 3     | 129.9                     | 12.4             | 13.4         | 7.6          | 871.0   | 545.5                                     | -37.5        | 22:50                    |

825

830

**Table 4** Observed and radar-driven simulated flow volume and peak discharge of Francolí River at the Tarragona hydrometric section for the control and test experiments. Negative values in relative errors denote model underestimation. Total rainfall amount is radar-derived and is expressed as the areal-averaged basin value. Time to peak refers on 22 October 2019.

835



840

845

850

| <b>Risk</b> | <b>Colour code</b> | <b>Accumulated rainfall threshold (mm/24 h)</b> | <b>Probability of occurrence</b> | <b>Numerical scale of risk</b> |
|-------------|--------------------|---|----------------------------------|--------------------------------|
| No          | Green              | –   | –                                | 0                              |
| Moderate    | yellow             | > 100   | Low                              | 1                              |
|             |                    |   | Medium                           | 2                              |
| High        | orange             | > 100   | High                             | 3                              |
|             |                    | > 200   | Low                              | 4                              |
| Very high   | red                | > 200   | Medium                           | 5                              |
|             |                    |   | High                             | 6                              |

**Table 5 Risk assessment and alert issuance according to the SMC**

855

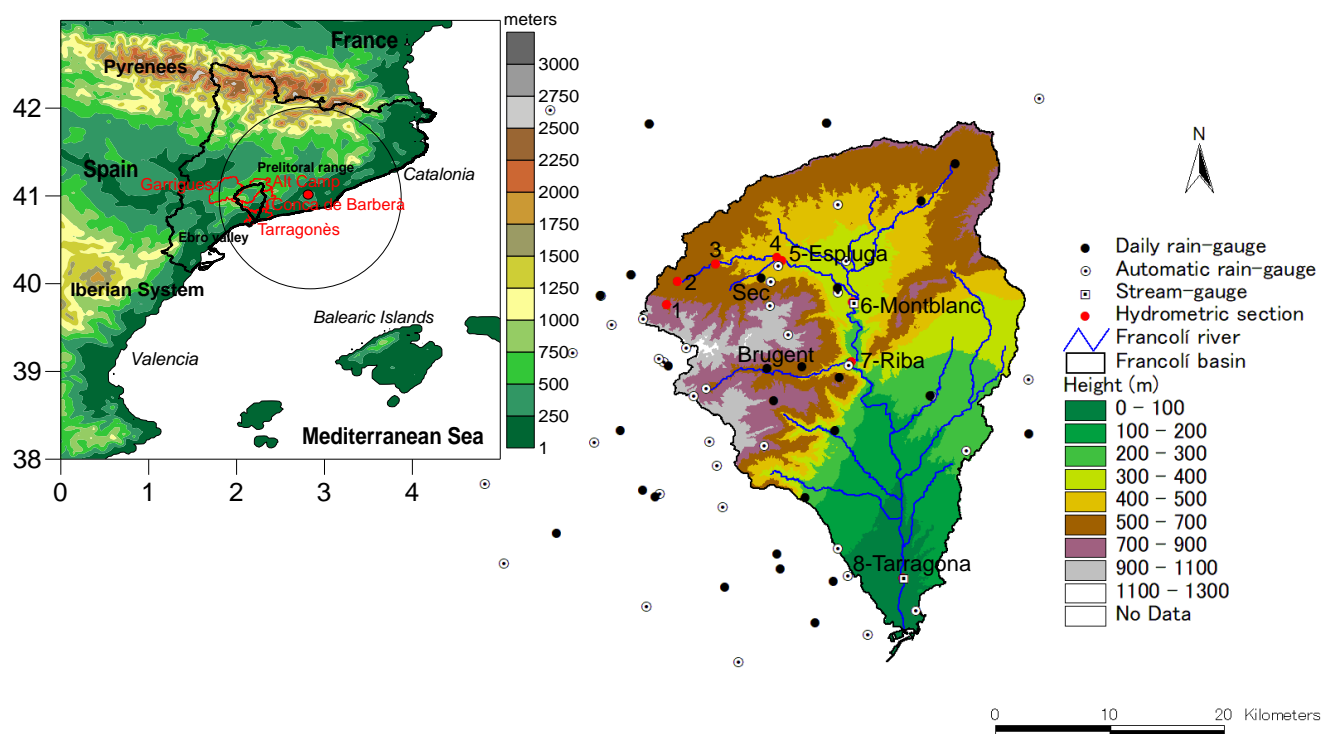
860

865



870

## FIGURES



875

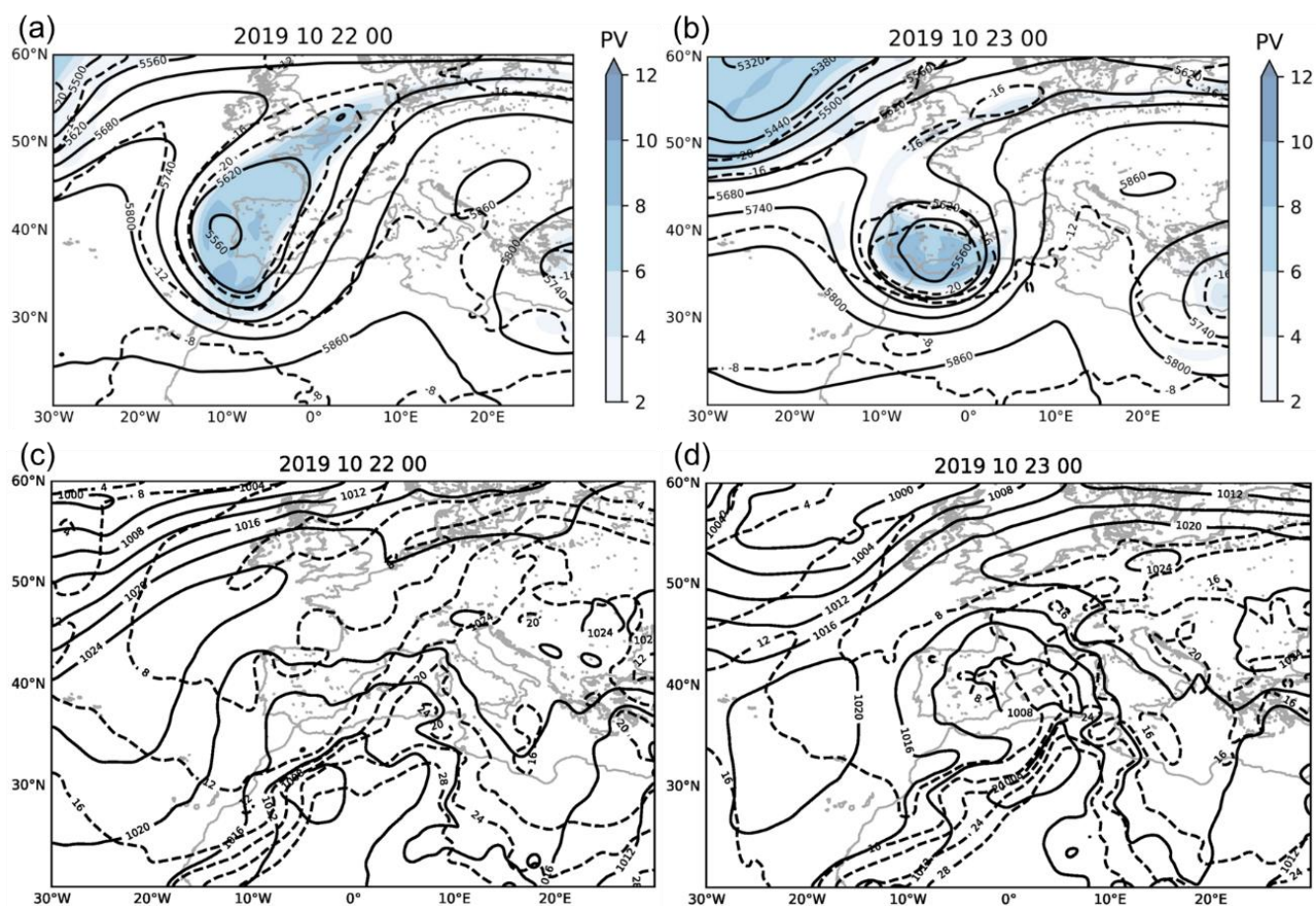
Figure 1. Top left: main geographical features of north-eastern coast of Spain. The location of the Barcelona weather radar from AEMET is shown as a red dot. The Francolí catchment is highlighted in thick black line. Radii of the radar circle is 100 km. The municipalities traversed by the Francolí river are also shown in red (further information in section 5.3). Centre left: main geographical features of the Francolí basin. The automatic rain-gauges are shown as white dots. Automatic stream-gauges are labelled and depicted as white squares. Daily pluviometers are illustrated as black dots. Hydrometric sections are denoted as red circles and labelled downstream (see Table 1 for further details).

880

885



890

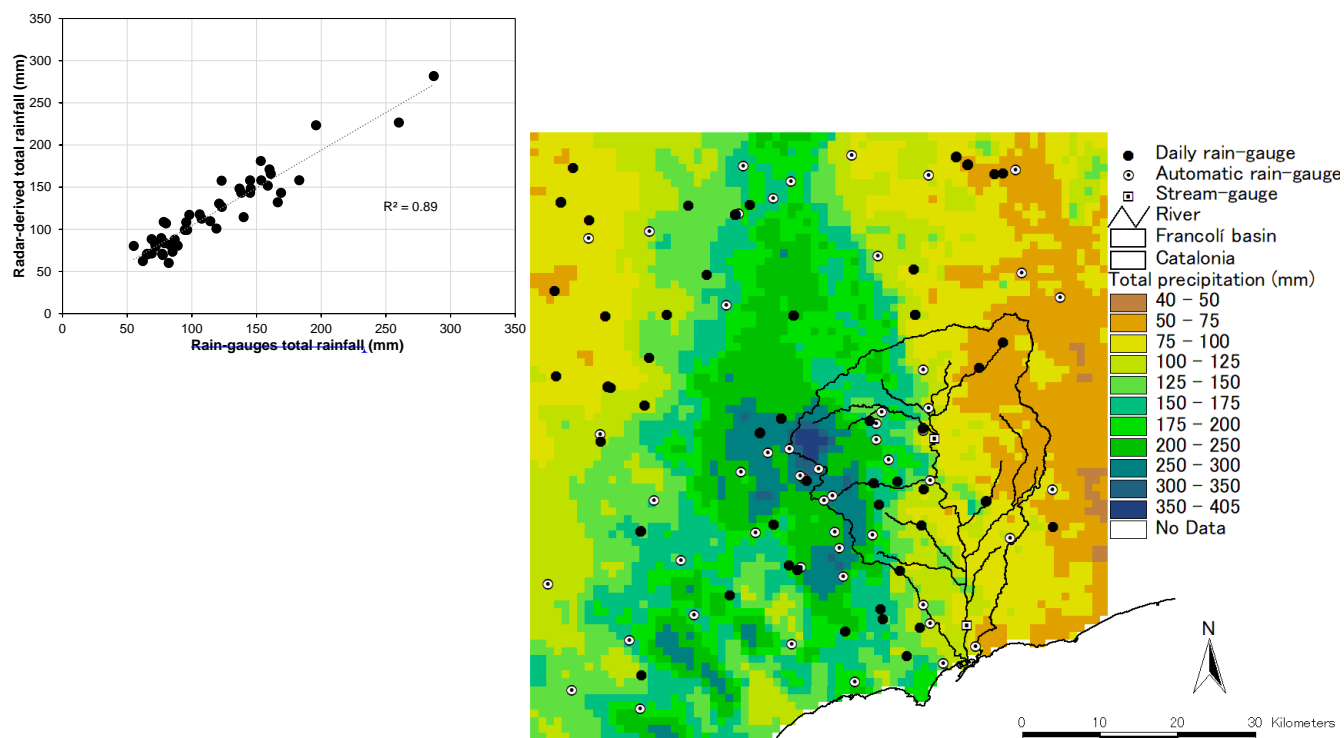


895 **Figure 2.** ECMWF analysis for geopotential height (solid lines, in gpm), temperature (dashed, in °C) at 500 hPa and 250-hPa potential vorticity (PVU, shaded in blue) on: (a) 22 and, (b) 23 October 2019 00:00 UTC. ECMWF analysis for mean sea level pressure (solid lines, hPa) and temperature at 850 hPa (dashed, in °C) on: (c) 22 and, (d) 23 October 2019 00:00 UTC.

900



905



910

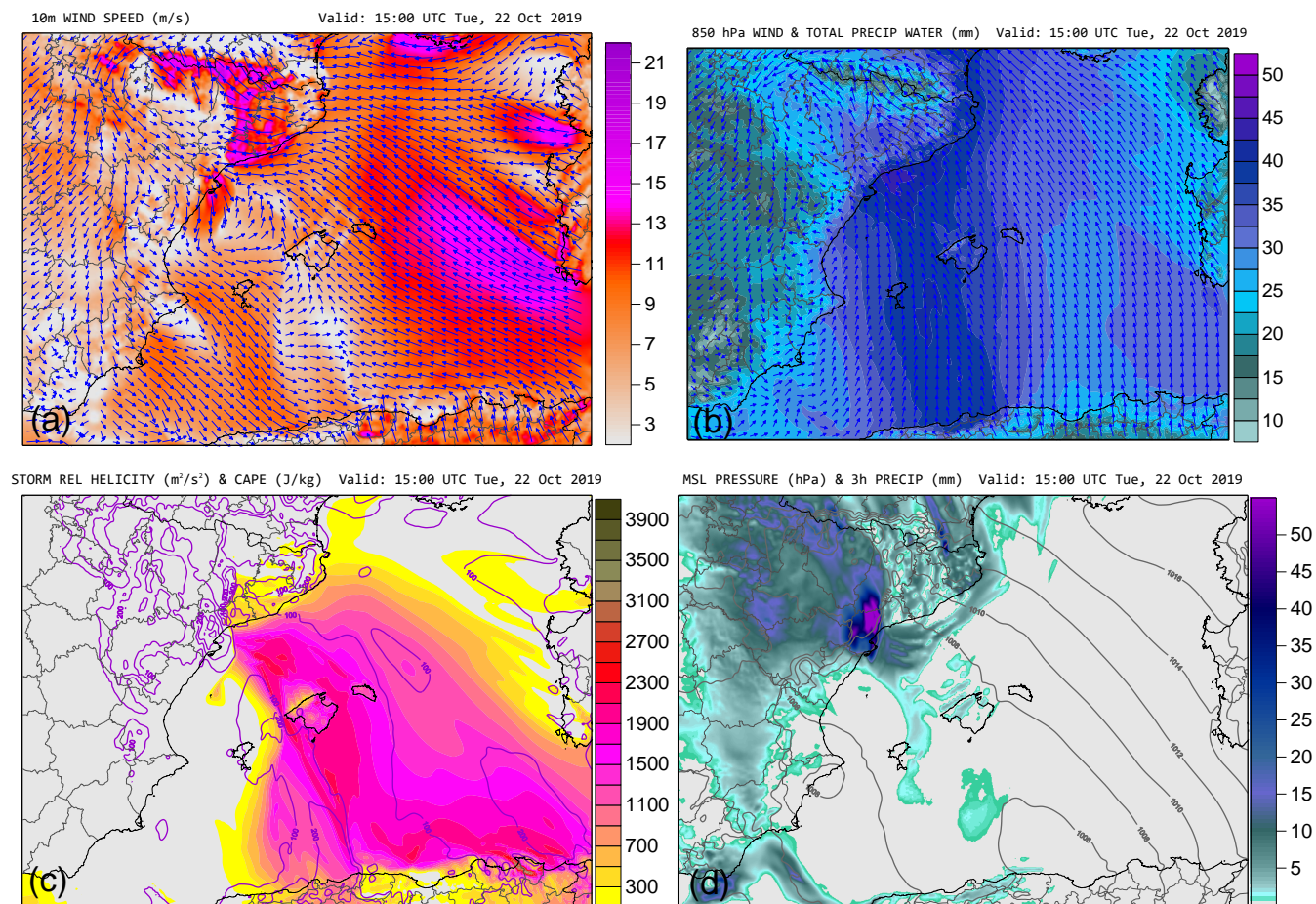
**Figure 3.** Top left: scatterplot of the 48 h radar-derived rainfall estimates against observed accumulations by the daily AEMET rain-gauge network over the selected region. Centre right: spatial distribution of the 48 h accumulated radar-estimated precipitation from 22 to 24 October 2019 at 00:00 UTC. The Francolí river catchment is highlighted with a thin black line. White squares stand for the automatic stream-gauges. White dots show the position of the automatic rain-gauges. Daily pluviometric stations are denoted by black dots.

915

920



925



930

**Figure 4.** Results of the control simulation at 15:00 UTC on 22 October 2019, showing: (a) surface wind field (m/s, according to scale); (b) 850 hPa wind vectors and precipitable water in the tropospheric column (mm, according to scale); (c) storm relative helicity ( $\text{m}^2/\text{s}^2$ , contours) and CAPE (J/kg, according to scale); and (d) sea level pressure (hPa, contours) and accumulated precipitation in previous 3 hours (mm, according to scale).

935



940

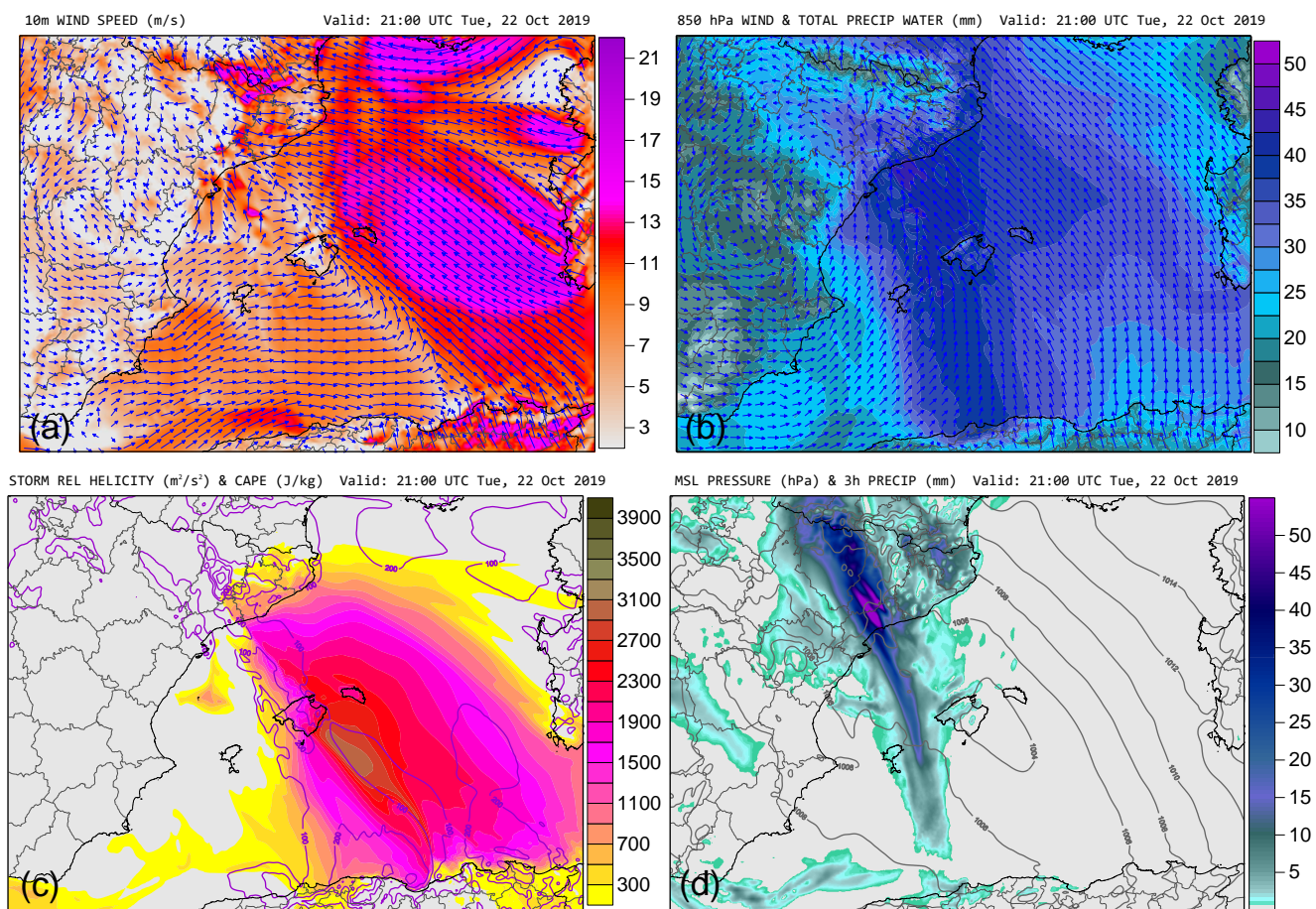


Figure 5. As in Fig. 4 but six hours later, at 21:00 UTC on 22 October 2019.

945

950



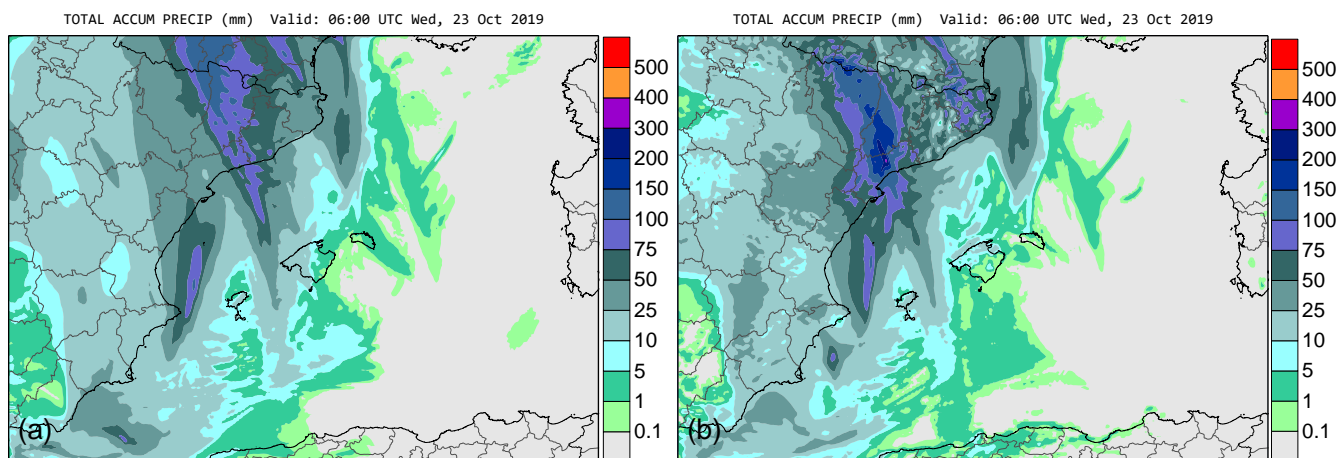


Figure 6. Comparison of **the model** simulated precipitation, accumulated in 24 h from 22 to 23 October 2019 at 06:00 UTC, between the (a) non-orographic and (b) full control simulations.

955

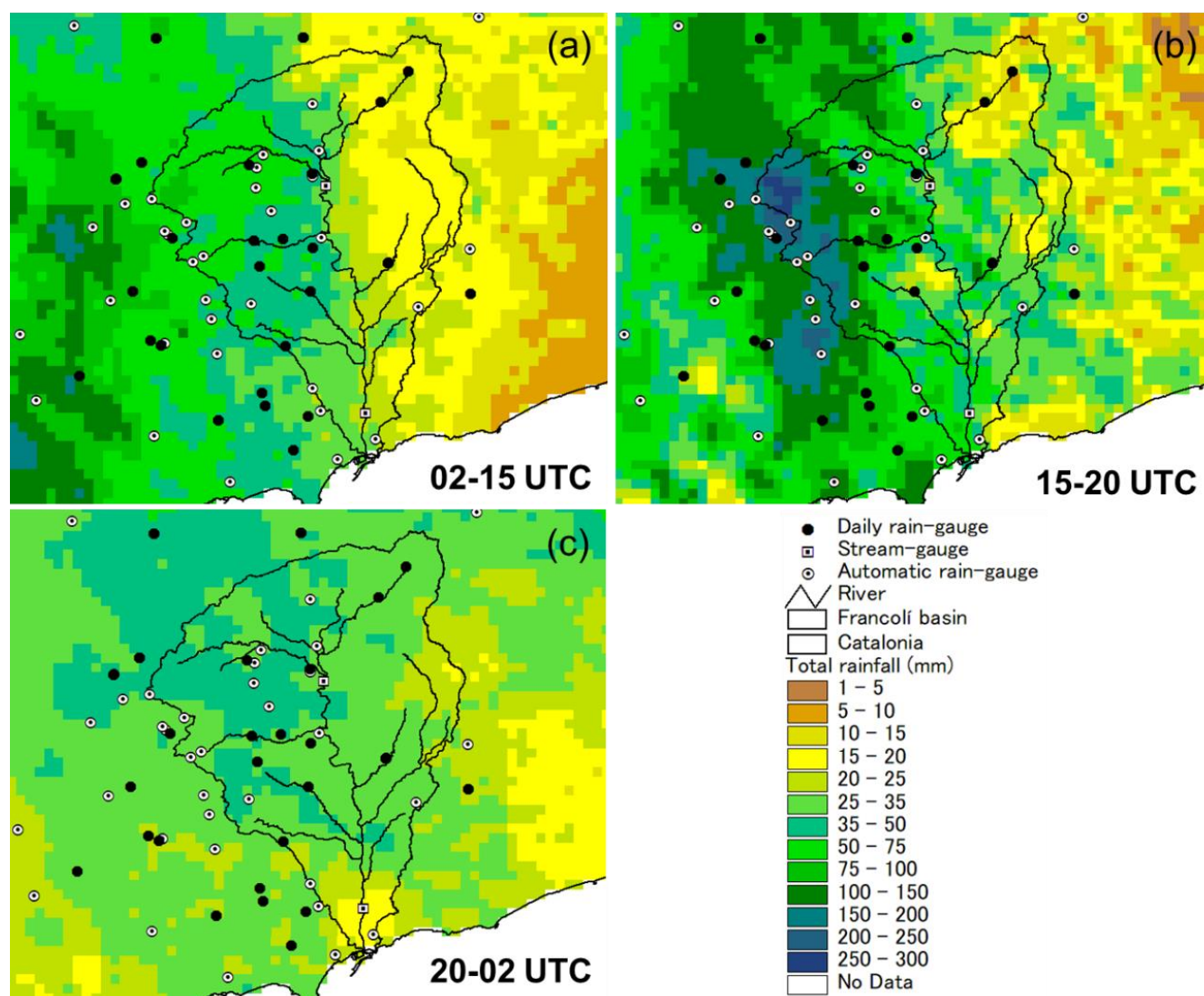
960

965

970



975

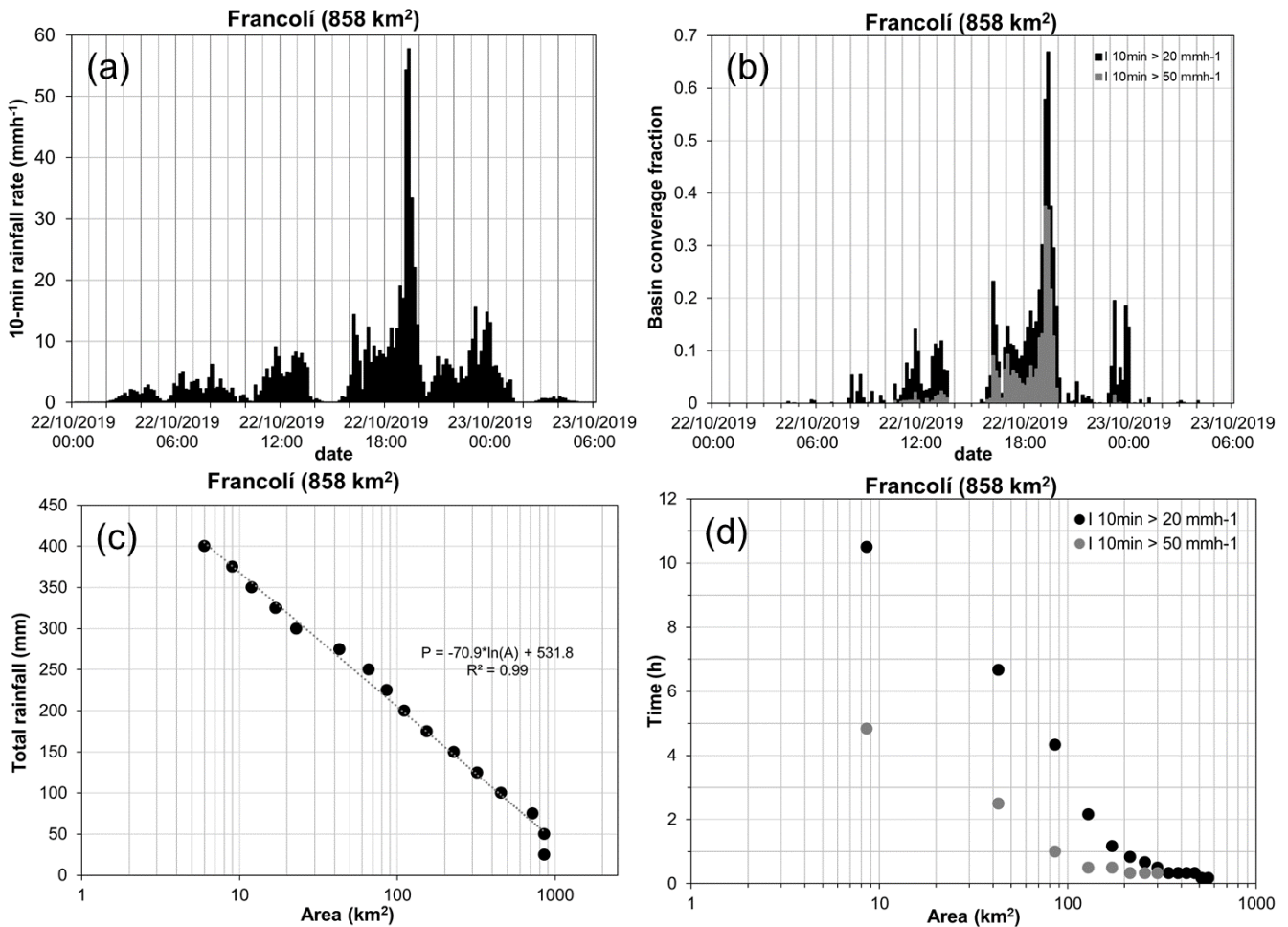


980

**Figure 7.** Spatial distribution of the accumulated radar-derived precipitation: (a) from 02:00 to 15:00 UTC on 22 October; (b) from 15:00 to 20:00 UTC on 22 October and; (c) from 20:00 UTC on 22 October to 02:00 UTC on 23 October. The Francolí river catchment is outlined with a thin black line. White squares represent the locations of automatic stream-gauges. White dots indicate the positions of automatic rain-gauges. Daily pluviometric stations are marked by black dots.



985

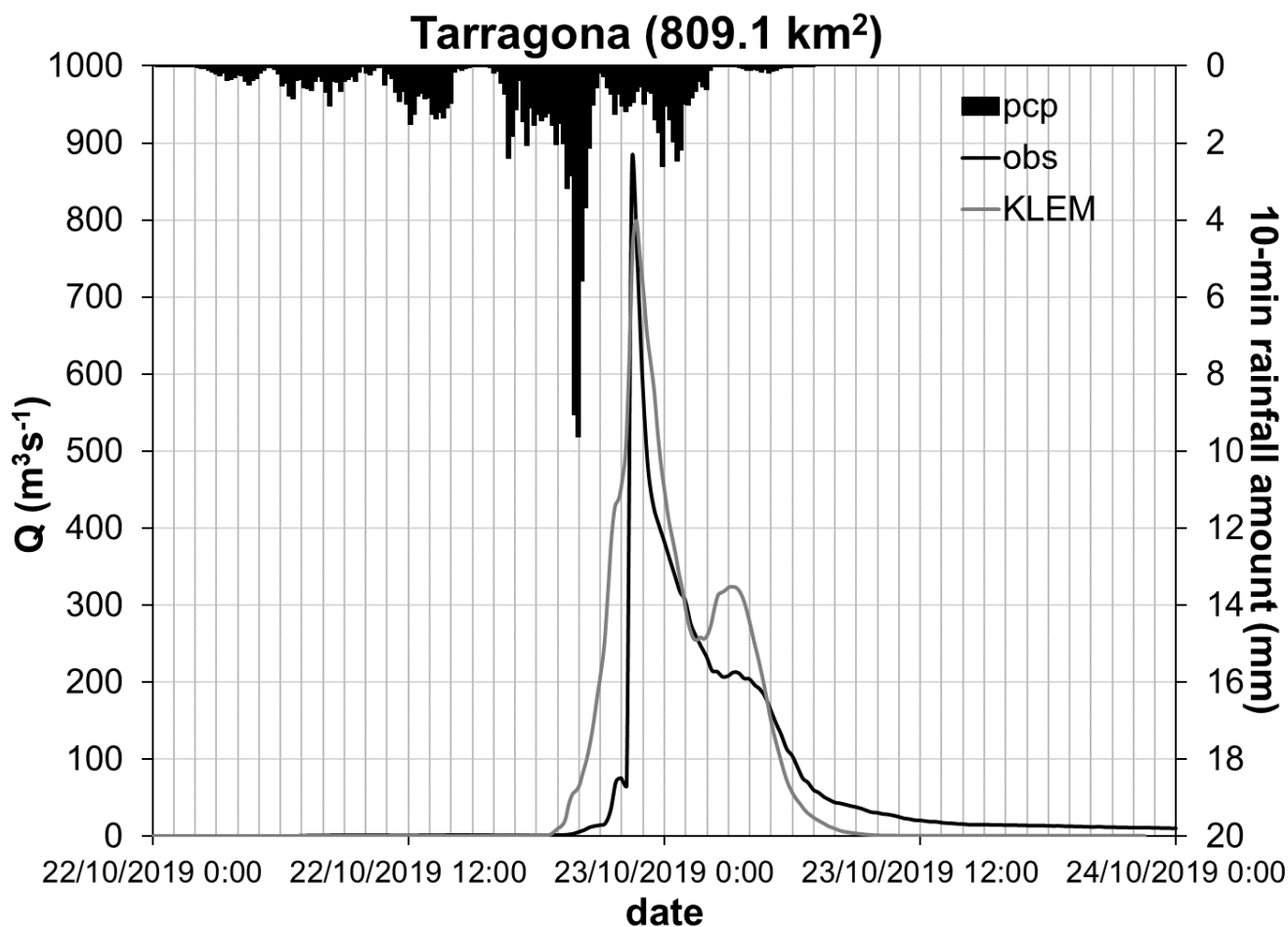


990 **Figure 8.** Time series from 00:00 UTC on 22 October to 06:00 UTC on 23 October showing the: (a) 10-min catchment-area average  
 rainfall, and; (b) fractional basin areas covered by 10-min precipitation rates  $>20 \text{ mmh}^{-1}$  (black bars) and  $>50 \text{ mmh}^{-1}$  (grey bars).  
 (c) Exceedance drainage extents above the indicated total precipitation thresholds, and; (d) relationship between the spatial and  
 temporal scales for 10-min rainfall rates  $>20 \text{ mmh}^{-1}$  (black dots) and  $>50 \text{ mmh}^{-1}$  (grey dots).

995



1000



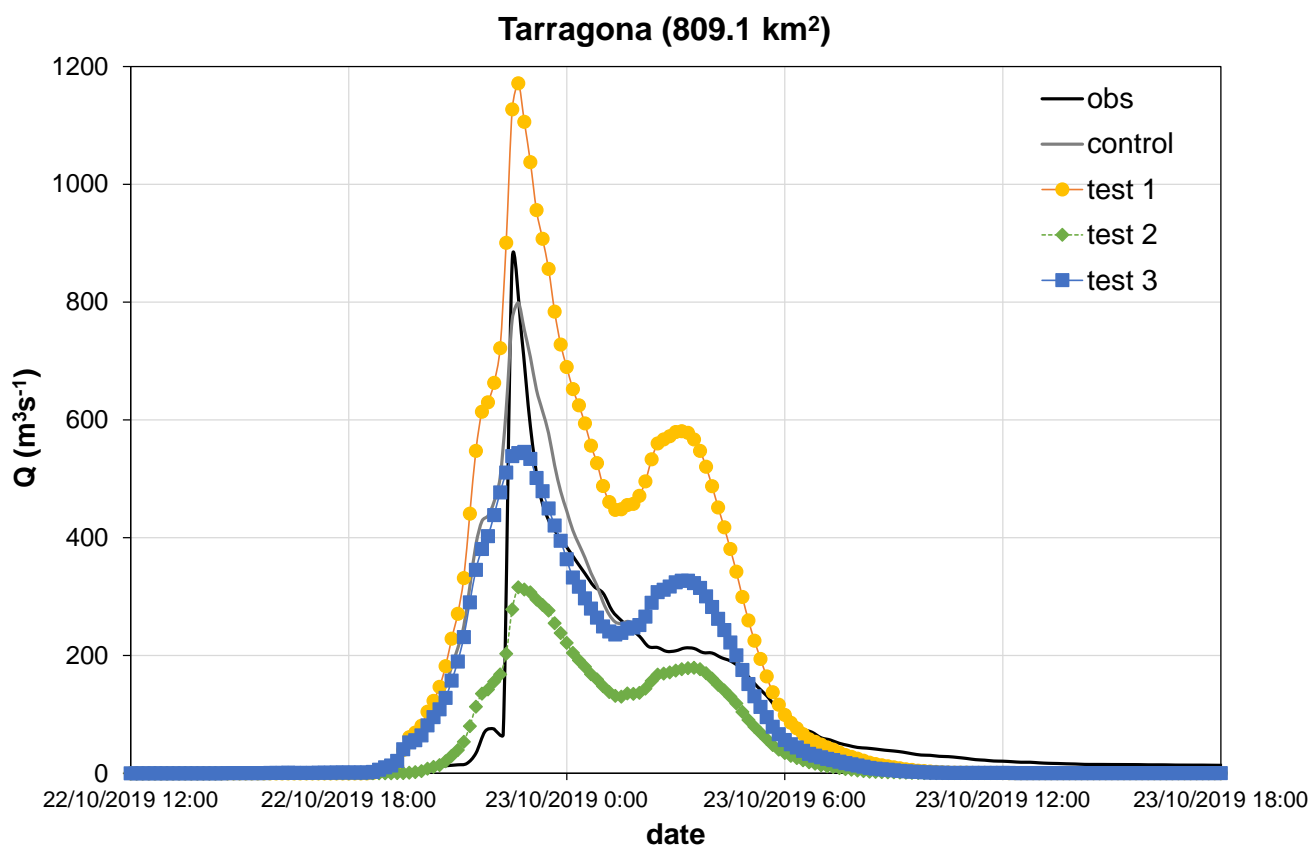
1005

Figure 9. Observed and KLEM radar-driven discharge simulation for the 22 October flash flood at the Tarragona flow-gauge. Also shown are the 10-min catchment-area average rainfall amounts enclosed by this hydrometric section.

1010



1015



**Figure 10.** Observed and radar-driven runoff simulations for the control and test experiments and the 22 October flash flood at the Tarragona flow-gauge in the Francolí basin.

1020

1025



1030

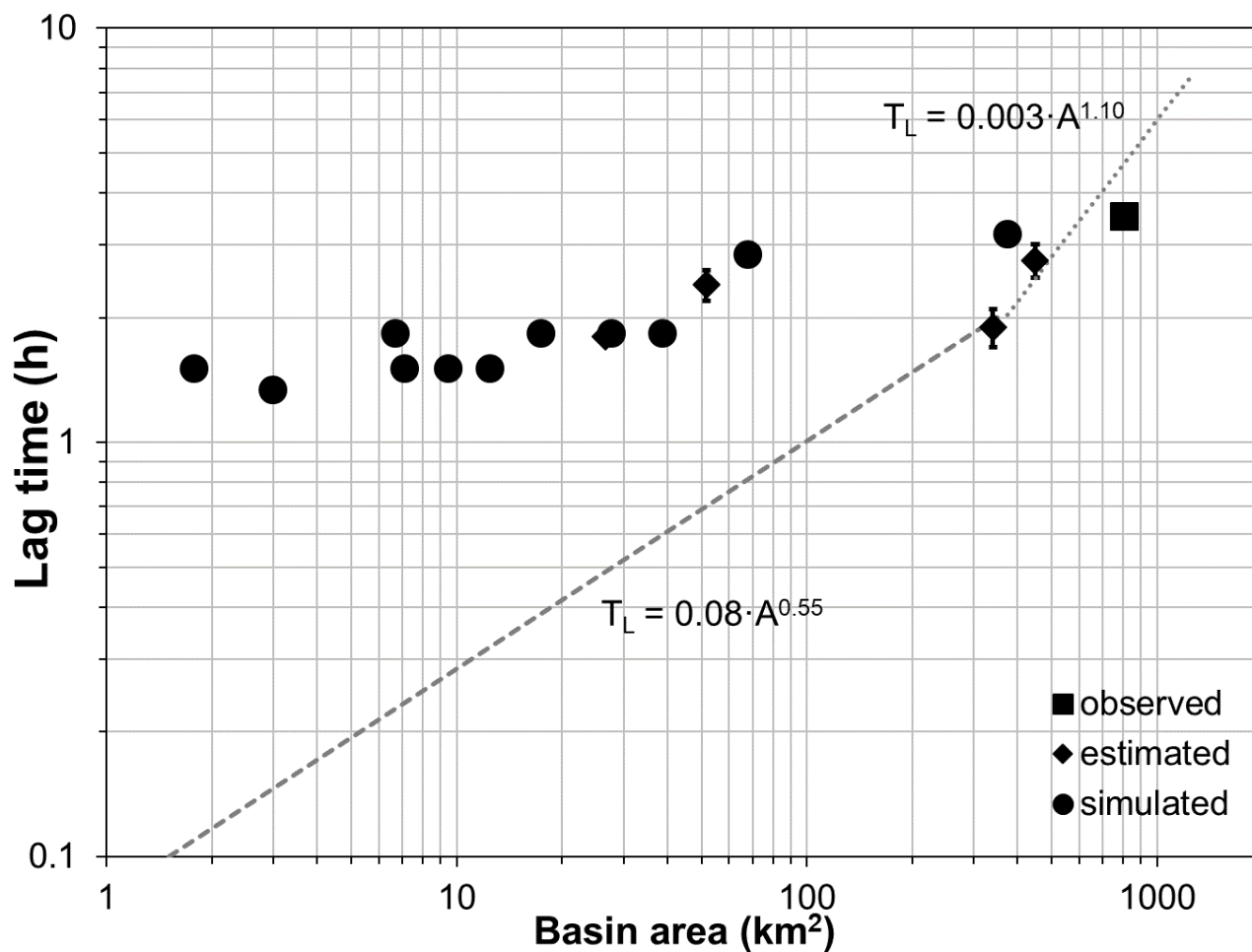
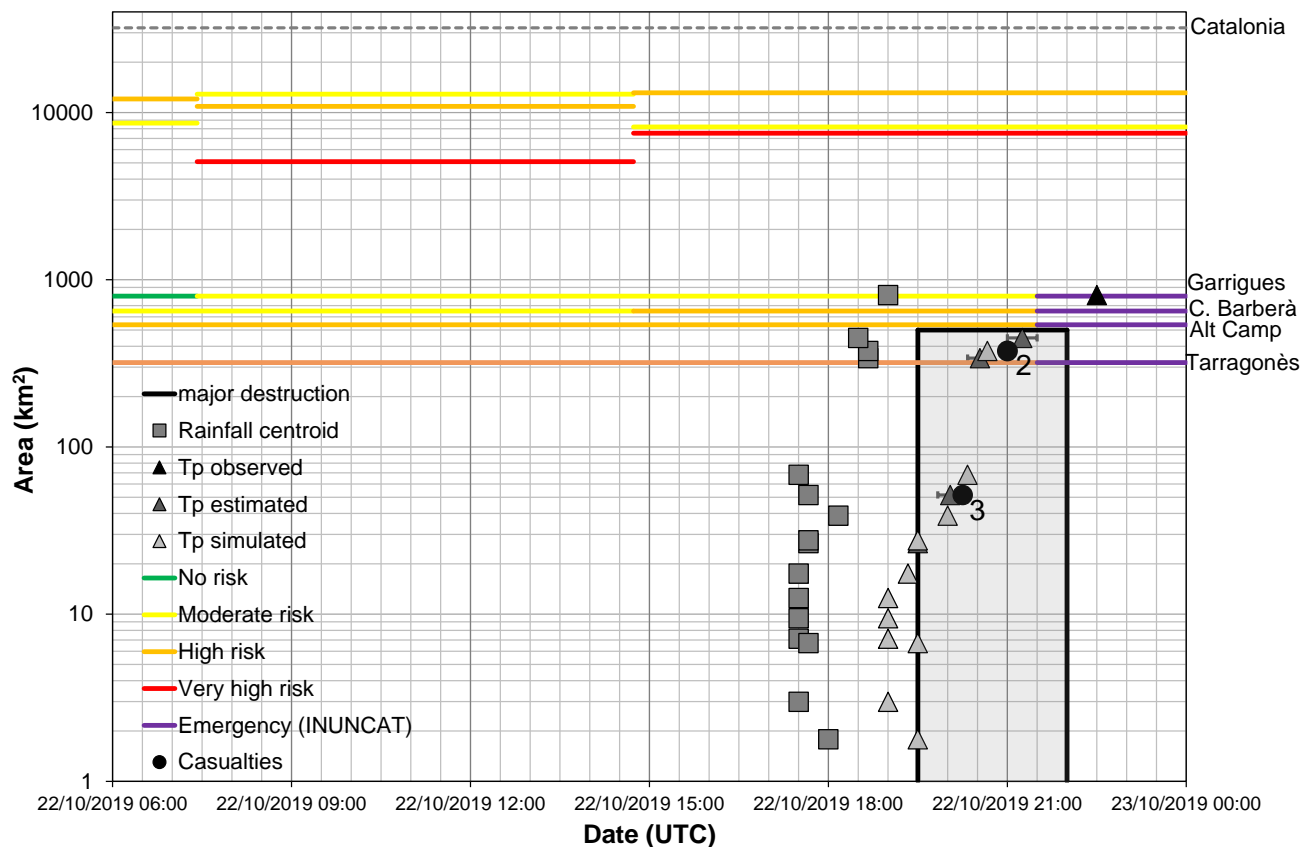


Figure 11. Lag time versus drainage area for the 22 October 2019 flash flood in the Francolí basin. Uncertainties in the estimated lag times are shown as vertical bars. Also shown the power-law relationships after Marchi et al. (2010).

1035



1040



1045 **Figure 12.** Catchment and social spatial and temporal scales during the catastrophic flash flood of the Francolí River on October 22, 2019. The number of casualties, timing and extent of the most devastating period of destruction (grey shaded area in the rectangle surrounded by thick black lines) are also indicated. Triangles in varying shades of grey represent observed, estimated and simulated times-to-peak (Tp). Uncertainties in the estimated times-to-peak are shown as horizontal bars. Squares denote the times of the rainfall hyetographs' centres of mass. Risk assessment and associated colour codes can be found in Table 5.

1050